Remote Sensing of Environment 246 (2020) 111890

Contents lists available at ScienceDirect

Remote Sensing of Environment

journal homepage: www.elsevier.com/locate/rse

Eutrophication changes in fifty large lakes on the Yangtze Plain of China derived from MERIS and OLCI observations

Qi Guan[a,b], Lian Feng[a,c,*], Xuejiao Hou[a], Guy Schurgers[b], Yi Zheng[a,c], Jing Tang[d,e]

[a] School of Environmental Science and Engineering, Southern University of Science and Technology, Shenzhen 518055, Guangdong, China
[b] Department of Geoscience and Natural Resource Management, University of Copenhagen, Copenhagen, Denmark
[c] Shenzhen Municipal Engineering Lab of Environmental IoT Technologies, Southern University of Science and Technology, Shenzhen 518055, Guangdong, China
[d] Department of Physical Geography and Ecosystem Science, Lund University, Lund, Sweden
[e] Department of Biology, University of Copenhagen, Copenhagen, Denmark

ARTICLE INFO

Keywords:
Chlorophyll-a
Algal bloom
Eutrophication
Yangtze Plain
Lakes
MERIS
OLCI
Water quality

ABSTRACT

The eutrophication problems in lakes on the Yangtze Plain of China have attracted global concern. However, a comprehensive assessment of the eutrophication status and its evolution is still lacking for these regional lakes, mostly because of technical difficulties and/or insufficient data to cover the large region. Our study attempts to fill this knowledge gap by using the entire archive of remote sensing images from two satellite ocean color missions (MEdium Resolution Imaging Spectrometer, or MERIS (2003 – 2011), and Ocean and Land Color Instrument, or OLCI (2017–2018)), together with in situ data on remote sensing reflectance and chlorophyll-a (Chla) concentrations across various lakes on the Yangtze Plain. A machine learning-based piecewise Chla algorithm was developed in this study, with special considerations to improve algorithm performance under lower Chla conditions. Remotely sensed Chla and algal bloom areas were then used to classify the eutrophication status of 50 large lakes on the Yangtze Plain, and the frequent satellite observations enabled us to estimate the probability of eutrophication occurrence (PEO) for each examined lake. The long-term mean Chla ranged from 17.58 mg m^{-3} to 43.86 mg m^{-3} on the Yangtze Plain, and severe floating algal blooms were found in 7 lakes. All 50 lakes had high climatological PEO values (50%) during the study period, indicating a generally high probability of eutrophication in lakes on the Yangtze Plain. However, 21 out of 51 lakes exhibited statistically significant ($p < .05$) decreasing trends in PEO during the observation period, suggesting an overall improvement in the water quality of lakes on the Yangtze Plain in recent years. The methods developed here are expected to contribute to real-time monitoring of drinking water safety for local regions, and the long-term results provide valuable baseline information for future lake conservation and restoration efforts.

1. Introduction

Lakes represent one of the most important components of the Earth's surface system, which provides us with a drinking water supply and provides critical ecological functions, such as irrigation, flood storage, fisheries, navigation, and recreation (Feng et al., 2013; Fu et al., 2003; Hou et al., 2017; Wang et al., 2014). This importance is particularly true for the Yangtze Plain of China, which holds more than 100 large lakes (area > 10 km^2), comprising ~30% of the total lake surface area in China. With the rapid population increase (with an increasing rate of 0.96% y^{-1} from 1990 to 2014) and economic growth (with a growth rate of 7.8% y^{-1} from 2005 to 2015) in the Yangtze basin (Luo et al., 2019), intensive anthropogenic activities bring unprecedented pressures to the regional environment, resulting in a series of environmental and ecological crises, including water quality deterioration (Feng et al., 2019; Hou et al., 2017), fishery reduction (Gong et al., 2005; Wang et al., 2014) and biodiversity loss (Fang et al., 2006; Fu et al., 2003; Huang and Li, 2016); these crises pose great threats to sustainable socioeconomic development in this region.

According to national lake surveys conducted from 2007 to 2011, severe eutrophication problems were identified in most of the lakes on the Yangtze Plain (Le et al., 2010; Xiao et al., 2007), as demonstrated by the higher chlorophyll-a (Chla) and nutrient concentrations (Xiao et al., 2007; Zhang et al., 2007; Zhang et al., 2008b); this problem attracted massive attention, and considerable efforts have been made on lacustrine water quality in these surveys (Ma et al., 2010a; Shi et al., 2007;

* Corresponding author at: School of Environmental Science and Engineering, Southern University of Science and Technology, Shenzhen 518055, Guangdong, China.
E-mail address: fengl@sustech.edu.cn (L. Feng).

https://doi.org/10.1016/j.rse.2020.111890
Received 7 December 2019; Received in revised form 5 May 2020; Accepted 11 May 2020

Zhang and Mei, 1996). The observed water quality deterioration was primarily attributed to the continuous increase in the input of pollutants into the lakes (Yang et al., 2010b), despite the considerable efforts that were made to control point and nonpoint sources of pollutions in the lakes' drainage basins (Wang et al., 2016).

Although remote sensing observations have been extensively used to examine the lake size dynamics (Ma et al., 2010b) during national lake surveys, water quality data have still been primarily obtained with traditional field sampling measurements (Yang et al., 2010b). Field sampling approach may be sufficient for small lakes with relative stable aquatic environments, while they often suffer from limitations related to the spatial and temporal representativeness of the data, preventing a comprehensive assessment of the changing water quality patterns over large areas and long periods. For example, due to complex optical variations across parts of a large lake (e.g., Poyang Lake and Dongting Lake), discrete point-level water samples may not well represent the true conditions of the entire lake. Furthermore, field measurements in different lakes may have been collected in different seasons or even different years, and rapid temporal variations prohibit a direct comparison of water quality between different lakes.

Due to their apparent advantages in large-scale research and their high frequency of observations, remote sensing techniques are increasingly being used to monitor the water quality of lakes on the Yangtze Plain in recent decades. Due to strong reflective satellite signals for highly turbid lakes on the Yangtze Plain (Feng et al., 2014a; Hou et al., 2017; Shi et al., 2015; Zhang et al., 2008a), the water clarity-related parameters (e.g., the total suspended sediments (TSS), water turbidity, and Secchi disk depth (Feng et al., 2019; Hou et al., 2017; Shi et al., 2015; Wang et al., 2011; Wu et al., 2008) of individual lakes or basin-scale lake clusters were quantified based on satellite observations; this information served as a first-order description of water quality and represented the visual perception of humans. However, these parameters provide limited information on the eutrophication status of these lakes.

Eutrophication-oriented studies mainly focus on tracing cyanobacterial blooms and attempt to assess the eutrophication status of a limited number of lakes on the Yangtze Plain. For example, two decades of Landsat observations were used to reconstruct the historical changes in the algal blooms in Taihu Lake (Duan et al., 2009), while more detailed descriptions of the short-term bloom dynamics were presented with the more frequent Moderate Resolution Imaging Spectroradiometer (MODIS) observations (Hu et al., 2010). Algal bloom areas and their spatiotemporal changes in Chaohu Lake have been mapped with similar methods as those used for Taihu Lake (Li et al., 2017; Zhang et al., 2016; Zhang et al., 2015). Moreover, efforts have been made to quantitatively retrieve the Chla or even the phycocyanin pigment concentrations based on in situ measurements and remote sensing images, and the developed algorithms ranged from empirical (Feng et al., 2014b; Garcia et al., 2006; Le et al., 2011; Min et al., 2017; Neil et al., 2019; Qi et al., 2014a; Song et al., 2013; Sun et al., 2009) to quasi-analytical (Duan et al., 2012; Garcia et al., 2006; Gitelson et al., 2008; Jiang et al., 2020; Le et al., 2009; Liu et al., 2020; Liu et al., 2018) approaches. Unfortunately, these previous bloom classification and Chla-retrieval studies generally focused on individual lakes, prohibiting a complete assessment of the eutrophication status of basin-scale lake groups. Indeed, the absence of such an assessment could be associated with the following two challenges:

1. The remote sensing data used in previous studies suffered from one or several limitations related to the spectral, radiometric and spatial resolutions. For example, with broad bands (band width of tens or even > 100 nm), the instruments (e.g., Landsat) or bands (high-resolution bands for MODIS and Visible Infrared Imaging Radiometer Suite (VIIRS)) designed for land applications may not be able to capture the narrow absorption/fluorescence and backscattering features of the Chla pigments (Smith et al., 2018). Likewise, these datasets have a relatively low signal-to-noise (SNR) ratio, and the smaller absorption/fluorescence and backscattering signals from Chla are difficult to resolve due to the overwhelming reflection caused by the high TSS concentrations in these lakes. In contrast, although they have high SNRs, typical ocean color satellite missions or bands (e.g., SeaWiFS and MODIS/VIIRS ocean bands) have spatial resolutions that are too coarse (1 km) to monitor inland waters (Feng et al., 2014b). Therefore, narrow bands with sufficient sensitivity are required to accurately retrieve Chla concentrations from turbid waters.
2. A lack of in situ data covering different water types (or optical properties) are available to develop a generic algorithm for the lakes across the entire Yangtze Plain. Previous remote sensing Chla algorithms were based on field-measured data from one or two lakes, and the developed algorithm may not be applicable in other lakes due to the potential differences in water optical properties. Although numerous field investigations have been conducted by different research groups and organizations in China, the level of data sharing between different entries is limited due to the absence of an effective mechanism, the possible differences in data measuring methods and the differences in measurement consistency.

Fortunately, the two satellite missions launched by the European Space Agency (ESA), the Medium Resolution Imaging Spectrometer (MERIS, 2002–2011) and Ocean and Land Color Instrument (OLCI, 2017-present), have unparalleled advantages in terms of spectral resolution (15 bands for MERIS and 21 bands for OLCI) and band width (~10 nm) over the other ocean color measurements; thus, these approaches can be used to detect the absorption features of Chla, particularly the absorption peak at ~665 nm and the Chla fluorescence at ~680 nm (Liu et al., 2020; Odermatt et al., 2010; Pahlevan et al., 2020; Qi et al., 2015; Soomets et al., 2020; Xue et al., 2019). Moreover, these two instruments provide 300-m full resolution observations, which make them useful for relatively small inland water bodies. Therefore, the complete datasets from these two missions were used in the current study to fill the current knowledge gap related to eutrophication and its long-term dynamics in the lakes on the Yangtze Plain with the following specific objectives:

1. Develop a generic Chla remote sensing algorithm that is applicable for lakes with various conditions on the Yangtze Plain and propose a practical approach and framework to quantify the eutrophication status of lakes using satellite-derived Chla and algal bloom areas;
2. Demonstrate the temporal and spatial dynamics of Chla and algal bloom areas for 50 large lakes on the Yangtze Plain using MERIS and OLCI imagery and assess the changes in the eutrophication conditions during the observational periods.

2. Study area and datasets

2.1. Study area

The Yangtze Plain is located in the middle and lower basin of the Yangtze River and has an area of ~7850,000 km^2 across five provinces and one municipality (Shanghai) (Hou et al., 2017; Wang et al., 2014). Lakes and ponds in this plain (elevation < 50 m above sea level) provide water for human consumption and agricultural/industrial development (Duan et al., 2014; Duan et al., 2012; Qin et al., 2007; Qin et al., 2010; Wang et al., 2005); additionally, they have vital roles in regulating local ecosystems and climate change (Feng et al., 2012a; Guan et al., 2018; Hou et al., 2017; Nakayama and Shankman, 2013; Tang et al., 2016). The Yangtze Plain lakes were generally formed by the sea level rise during the postglacial period when the water level of the Yangtze River elevated to inundate the lowland regions, resulting in shallow lakes (a mean water depth of < 5 m) (Yang et al., 2008). Furthermore, the ecosystems of the lakes have been disturbed by extensive human activities (Du et al., 2011; Fang et al., 2005; Feng et al., 2012b; Ma et al., 2010a) and accelerated urbanization (Wang et al., 2014; Zhao et al., 2005). These lakes suffer from a range of severe environmental issues, including reduced inundation (Feng et al., 2012a; Feng et al., 2013; Yin et al., 2007), water quality decline (Feng et al., 2019; Hou et al., 2017), and wetland degradation (Feng et al., 2016; Han et al., 2015).

As a result of severe water eutrophication, cyanobacterial blooms frequently occur in several lakes on the Yangtze Plain. Most recently, in the summer of 2007, a severe algal bloom occurred in Taihu Lake and was extensively covered by the media; this severe algal bloom produced a drinking water crisis for two million citizens in Wuxi City, Jiangsu Province (Duan et al., 2014; Duan et al., 2009; Qin et al., 2007). Similarly, frequent cyanobacterial blooms occurred in Chaohu Lake, posing a serious threat to the drinking water resources of Heifei City, which has a population of ~8 million (Xie et al., 2010). Additionally, water eutrophication has been found in other lakes on the Yangtze Plain during national lake surveys (Le et al., 2010; Xiao et al., 2007), indicating that eutrophication has become one of the main potential environmental crises for lakes on the Yangtze Plain. As the focal lakes of water eutrophication throughout the Yangtze Plain, many attempts have been made to quantify the Chla concentration and eutrophication status distributions for Chaohu and Taihu lakes (Hu et al., 2010; Qi et al., 2014b; Qin et al., 2007; Sun et al., 2009; Tao et al., 2015; Zhang et al., 2015; Zhang et al., 2016). However, the water eutrophication status and algal bloom status of most other lakes are still unknown. The eutrophication conditions of 50 large lakes in the Yangtze Plain were studies here, and the basic information of each lake is shown in Table 1.

2.2. Satellite data and preprocessing

The entire mission (2003–2011) of the MERIS satellite images covering the study region was obtained from the NASA Goddard Space Flight Center (https://oceancolor.gsfc.nasa.gov/), and the OLCI images between 2017 and 2018 were downloaded from the Copernicus Data and Information Access Service. Full resolution data (300 m) were used from both instruments, and in total, 1672 and 552 images were obtained from MERIS and OLCI, respectively. All MERIS and OLCI images were processed with SeaDAS software (version 7.4) to produce the Rayleigh-corrected reflectance (R_{rc}). The calculation of R_{rc} for each wavelength (λ) is expressed as follows:

$$R_{rc,\lambda} = \pi L_{t,\lambda'}/(F_0 \times \cos\theta_0) - R_{r,\lambda} \quad (1)$$

where F_0 is the extraterrestrial solar irradiance, $R_{r,\lambda}$ is the reflectance from Rayleigh (molecular) scattering, L_t is the gaseous absorption-corrected sensor radiance, and θ_0 is the solar zenith angle. Although this method only partially removes the atmospheric radiance, R_{rc} has been considered to be effective in various aquatic environmental monitoring studies, and particularly for algal bloom detection (Hu, 2009; Hu et al., 2010).

To further quantitatively retrieve the Chla concentrations, the impacts of aerosol scattering in R_{rc} should be removed. Although it is more straightforward to apply the SeaDAS-embedded atmospheric correction approaches over the MERIS and OLCI images (Gordon and Wang, 1994), the resulting remote sensing reflectance (R_{rs}) spectra were problematic due to their unrealistic spectral shapes (see Fig. S1). Instead, the POLYMER (i.e., a polynomial-based approach originally designed for MERIS) atmospheric algorithm was employed in this study to generate the full atmospherically corrected R_{rs} (Steinmetz et al., 2011; Steinmetz et al., 2016), where the resulting R_{rs} retrievals showed much better agreement with the in situ data than the datasets obtained using SeaDAS-embedded correction method based on spectral shapes and reflectance magnitudes. The POLYMER algorithm simulates atmospheric contributions of satellite signals using a spectral optimization scheme, where optical parameters are iteratively fed into bio-optical models, resulting in optimal R_{rs} values and aerosol contributions. Previous validations of the POLYMER algorithm have also demonstrated satisfactory performance in terms of producing accurate R_{rs} values for MERIS, OLCI and other ocean color instruments (Müller et al., 2015; Mograne et al., 2019; Pereira-Sandoval et al., 2019; Qin et al., 2017; Steinmetz and Ramon, 2018; Warren et al., 2019; Zhang et al., 2018). POLYMER also outperforms the NASA standard atmospheric correction method in data coverage due to its higher tolerance to unfavorable conditions (e.g., sun glint and thin clouds) (Zhang et al., 2018). Note that during POLYMER atmospheric correction process, the normalized sun glint coefficient (L_{gn}, sr^{-1}) for each pixel was also estimated using the method proposed by Cox and Munk (1954) and pixels with $L_{gn} > 0.04$ (Zhang et al., 2018) were considered sun glint contaminated and discarded in further analysis. All satellite images were then re-projected into the same cylindrical equidistance (rectangular) projection to further facilitate the generation and analysis of the Chla products. Although the OLCI instrument provides more spectral bands than MERIS, only the common wavelengths (i.e., 620, 665, 681, 709 and 754 nm) of the two instruments were used in this study to derive the Chla concentrations of the Yangtze Plain lakes.

2.2.1. In situ datasets

Field measurements of Chla concentrations and R_{rs} spectra were collected from 11 large lakes (Fig. 1) on the Yangtze Plain. These field surveys were conducted across four different seasons from 2005 to 2018, and the data represent various water conditions. The hyperspectral R_{rs} spectra were measured with a PSR + 3500 field portable spectroradiometer (Spectral Evolution Inc. (SEI)), which has a spectral range of 350–2500 nm. The NASA-recommended ocean optics protocol (Mobley, 1999) was followed when conducting above-water R_{rs} measurements, and the upward radiance (L_u), download sky radiance (L_{sky}) and radiance from a standard reference plaque (L_{pla}) were measured. These hyperspectral radiance measurements were converted into MERIS/OLCI-equivalent bands using their relative spectral response functions. Then, R_{rs} for each MERIS/OLCI band ($R_{rs,\lambda}$) was calculated as follows:

$$R_{rs,\lambda} = \rho_{f,\lambda}\,(L_{u,\lambda} - \rho_{f,\lambda} \times L_{sky,\lambda})/\pi L_{pla,\lambda} \quad (2)$$

where ρ_{pla} is the reflectance of the standard reference plaque (~10%), and ρ_f is the Fresnel reflection of the water surface, which was assumed to be 0.022 for a flat-water surface (Mobley et al., 2003). Note that, although the Fresnel reflection wavelength is also a function of wavelength, the application of a spectral optimization method to account for such impacts (Lee et al., 2010) resulted in incorrect spectral shapes and magnitudes. As such, the constant (0.022) was used for in situ R_{rs} calculations and wavelength-dependent values were not considered.

Samples were collected at the water surface (depth of < 0.5 m) wherever the R_{rs} spectrum was measured. The water samples were filtered through 0.45-μm Whatman cellulose acetate membrane filters; filters were soaked with 90% acetone and then stored at 0° for 24 h. An RF-5301 fluorescent spectrophotometer (Shimadzu, Kyoto, Japan) was calibrated with Chla standards and used to measure the Chla concentration (mg m^{-3}). Digital photos were taken for all sampled sites to record whether algal blooms or submerged vegetation occurred in these locations. Water samples with severe cyanobacterial blooms (i.e., apparent surface scums) or aquatic vegetation were excluded for Chla algorithm development, and a total of 604 pairs of in situ R_{rs} spectra and Chla concentrations were used to derive the Chla algorithm. Field-measured Rrs spectra and Chla concentrations were plotted in Fig. 2a. Furthermore, the corresponding total suspended sediments (TSS) were also shown in Fig. 2b and Table 2.

2.2.2. Ancillary datasets

Meteorological data, including precipitation and temperature, were obtained to examine the potential impacts of natural drivers on the long-term change patterns of Chla. The monthly precipitation data from

Table 1
General information (names, locations, mean areas), and the satellite-derived climatological mean Chla and PEO of the 50 examined lakes in this study. Also listed are the correlation coefficients between long-term PEO and concurrent conditions of potential driving factors (temperature, precipitation, chemical fertilizer, industrial wastewater and biological excrement), and the numbers in the parenthesis are the relative contributions (in percentage) of these factors to the interannual changes in the PEO (estimated using a multiple general linear model regression). Statistically significant (i.e., $p < .05$) correlations and contributions are annotated with "*".

ID	Name	Lon	Lat	Area (km^2)	Chla (mg/m^3)	PEO (%)	Fertilizer	Excrement	Wastewater	Temperature	Precipitation
L01	Beimin	111.87	29.71	14.25	30.70	88.52	−0.18 (3.40)	−0.19 (0.45)	0.38 (14.79)	0.05 (19.28)	−0.60* (16.71)
L02	Xihu	111.94	29.36	40.00	37.42	91.07	0.46 (21.50)	0.27 (8.55)	−0.18 (5.06)	0.73* (39.17*)	−0.34 (4.87)
L03	Shanpo	112.03	29.43	18.83	26.54	89.12	−0.29 (8.42)	−0.49 (25.14)	0.58* (19.60)	0.32 (2.84)	−0.61* (22.12)
L04	Changhu	112.4	30.44	114.03	29.79	87.01	0.38 (14.51)	0.29 (1.74)	0.22 (0.05)	0.13 (4.19)	−0.21 (33.17)
L05	Datong	112.51	29.21	83.10	20.57	75.43	−0.50 (24.72)	−0.57* (13.37)	0.86* (35.68*)	−0.33 (10.72)	−0.03 (0.24)
L06	Donghu (CD)	112.64	29.37	24.85	29.86	89.48	−0.26 (6.95)	−0.16 (4.26)	0.09 (0.36)	−0.34 (12.19)	0.27 (0.26)
L07	Dongting	113.12	29.34	2614.36	22.79	69.73	0.05 (0.23)	−0.15 (6.51)	0.16 (7.19)	−0.28 (0.30)	−0.21 (12.77)
L08	Honghu	113.34	29.86	340.05	32.13	89.84	0.25 (6.38)	0.14 (4.02)	−0.07 (5.43)	−0.25 (24.96)	−0.08 (4.98)
L09	Longsai	113.51	30.84	9.34	29.46	87.64	0.55* (30.16)	−0.10 (22.82)	0.13 (2.28)	0.02 (1.58)	−0.57* (7.06)
L10	Huanggai	113.55	29.7	59.47	34.91	94.81	−0.72* (52.17*)	−0.57* (0.14)	0.46 (23.06)	−0.22 (8.22)	−0.08 (0.28)
L11	Wuhu (XT)	113.8	30.18	32.93	32.56	86.50	−0.35 (12.36)	−0.08 (4.71)	0.06 (42.69)	0.21 (2.20)	−0.03 (0.80)
L12	Yezhu	114.07	30.86	25.88	29.62	92.03	−0.13 (1.64)	−0.43 (18.89)	0.52 (12.18)	0.66* (13.30)	−0.40 (13.58)
L13	Xiliang	114.08	29.95	28.58	35.46	90.53	−0.21 (4.29)	−0.60* (54.28*)	0.92* (30.88*)	0.58* (1.78)	−0.46 (4.74)
L14	Luhu	114.2	30.22	47.33	25.80	83.38	0.83* (68.50*)	0.66* (1.79)	0.20 (17.40)	0.24 (0.21)	−0.68* (1.80)
L15	Futou	114.23	30.02	141.22	28.86	87.58	0.79* (62.67*)	0.34 (28.02*)	0.29 (1.55)	0.27 (0.00)	−0.32 (0.00)
L16	Houhu	114.28	30.74	12.61	28.60	85.61	0.38 (14.24)	0.02 (4.69)	0.43 (12.81)	0.39 (14.73)	−0.28 (0.00)
L17	Tangxun	114.36	30.42	44.83	33.14	90.25	0.79* (61.69*)	0.55* (0.07)	0.10 (25.31*)	0.34 (0.65)	−0.86* (5.89)
L18	Donghu (WH)	114.4	30.56	34.35	37.35	89.94	0.89* (80.01*)	0.81* (7.66)	0.78* (7.16)	0.41 (0.41)	−0.42 (0.13)
L19	Wuhu (WH)	114.49	30.81	27.5	28.83	89.20	0.93* (87.13*)	0.70* (1.02)	0.77* (5.54*)	0.56* (30.8*)	−0.56* (2.39*)
L20	Liangzi	114.51	30.23	351.77	25.77	79.88	0.91* (82.58*)	0.48 (2.34*)	0.25 (13.48*)	0.31 (1.43*)	−0.69* (0.04)
L21	Baoxie	114.58	30.38	17.75	37.13	94.65	0.40 (16.03)	−0.14 (0.27)	0.19 (8.30)	−0.04 (3.81)	0.04 (35.61)
L22	Zhangdu	114.7	30.65	36.24	28.68	91.88	0.30 (9.15)	0.37 (4.86)	−0.29 (39.00)	0.18 (3.68)	−0.39 (0.08)
L23	Baoan	114.71	30.25	38.71	26.00	84.87	0.59* (34.70*)	0.59* (13.93)	0.01 (0.18)	0.27 (9.06)	−0.05 (23.53)
L24	Wusi	114.71	30.45	12.00	29.86	91.71	−0.64* (40.39*)	0.18 (0.17)	−0.58* (0.63)	0.14 (13.25)	0.71* (22.12)
L25	Yaer	114.72	30.46	12.64	34.49	86.94	0.96* (93.04*)	0.34 (0.06)	0.53 (0.67)	0.45 (1.31)	−0.79* (0.33)
L26	Sanshan	114.77	30.31	17.83	31.71	89.96	0.89* (78.55*)	−0.19 (0.01)	0.73* (0.26)	0.20 (6.66)	−0.74* (0.14)
L27	Daye	115.1	30.1	73.65	30.14	89.09	0.31 (9.64)	0.69* (39.22*)	0.01 (6.66)	−0.45 (17.32)	−0.15 (4.46)
L28	Wanghu	115.33	29.87	42.87	24.89	81.86	0.84* (69.73*)	0.68* (6.10)	−0.62* (3.47)	−0.25 (5.84)	0.26 (0.62)
L29	Wushan	115.59	29.91	15.11	43.86	95.98	0.27 (7.27)	−0.43 (37.60*)	0.64* (7.32)	0.28 (8.34)	0.08 (17.40)
L30	Chihu	115.69	29.78	35.9	35.74	91.44	0.23 (5.40)	−0.22 (2.41)	−0.37 (30.55)	0.28 (8.81)	−0.19 (0.76)
L31	Taibai	115.81	29.97	27.42	28.24	93.47	0.56* (31.22*)	−0.16 (20.62)	0.39 (21.78)	−0.05 (12.42)	−0.47 (0.13)
L32	Saihu	115.85	29.69	53.33	25.66	87.68	0.37 (13.78)	−0.19 (0.56)	0.36 (53.86*)	0.12 (5.05)	−0.44 (0.37)
L33	Xiayao	116.06	28.69	16.1	28.96	94.85	−0.36 (13.24)	−0.72* (41.32*)	−0.20 (11.48)	−0.45 (17.57)	−0.35 (1.52)
L34	Longgan	116.15	29.95	280.48	22.88	83.85	0.47 (21.98)	0.47 (8.64)	−0.58 (29.98*)	0.43 (26.77*)	−0.04 (0.80)
L35	Poyang	116.67	29.14	3206.98	24.75	78.12	0.16 (2.54)	0.06 (0.27)	0.09 (0.16)	−0.17 (4.25)	0.19 (3.31)
L36	Wuchang	116.69	30.28	112.02	26.02	91.45	0.25 (6.32)	−0.25 (0.87)	0.28 (2.66)	0.50 (37.33)	−0.47 (0.18)
L37	Caizi	117.07	30.8	171.59	28.04	90.26	0.66* (43.69*)	−0.78* (22.81)	−0.21 (15.69)	0.27 (1.36)	0.07 (0.06)
L38	Shengjin	117.07	30.38	96.09	30.61	92.76	−0.34 (11.23)	0.34 (1.17)	0.08 (11.13)	0.63* (28.93*)	−0.91* (40.77*)
L39	Baidang	117.38	30.81	38.69	27.01	85.54	−0.20 (3.84)	−0.32 (60.55*)	−0.17 (5.48)	0.07 (8.62)	−0.17 (1.70)
L40	Chaohu	117.53	31.57	786.01	21.07	83.06	0.38 (14.68)	−0.13 (9.41)	0.33 (2.37)	0.27 (4.59)	−0.54* (23.50)
L41	Shijiu	118.88	31.47	178.04	30.65	91.04	−0.38 (14.78)	−0.23 (0.00)	0.28 (3.16)	−0.28 (25.11)	−0.59* (14.33)
L42	Gucheng	118.92	31.28	27.9	34.09	86.15	0.33 (11.19)	0.33 (0.32)	0.47 (21.46)	−0.04 (3.25)	−0.85* (47.96*)
L43	Nanyi	118.96	31.11	197.83	22.64	89.33	0.45 (20.11)	−0.27 (10.84)	0.80* (33.80)	0.07 (2.80)	−0.12 (0.01)
L44	Changdang	119.55	31.62	84.33	29.56	94.83	−0.25 (6.14)	0.12 (4.95)	0.36 (17.48)	−0.27 (23.12)	−0.09 (2.26)
L45	Xijiu	119.8	31.37	11.18	26.37	93.36	0.75* (59.31*)	−0.80* (4.62)	0.43 (0.18)	−0.09 (3.12)	−0.46 (2.71)
L46	Gehu	119.81	31.6	139.56	39.09	95.87	0.70* (49.31*)	−0.60* (0.30)	−0.15 (7.38)	−0.55* (17.82)	−0.48 (11.36)
L47	Taihu	120.19	31.2	2537.17	17.58	73.37	0.22 (5.01)	0.19 (0.45)	0.46 (34.53)	0.16 (0.19)	−0.09 (9.47)
L48	Yangcheng	120.77	31.43	123.6	25.77	83.95	0.67* (45.47*)	0.85* (26.63*)	0.59* (2.89)	−0.31 (13.76)	−0.90* (3.71)
L49	Chenghu	120.82	31.21	37.11	25.23	83.32	0.89* (79.29*)	0.81* (0.95*)	0.55* (4.58)	0.17 (2.29)	−0.78* (1.90)
L50	Dianshan	120.96	31.12	63.71	23.12	79.23	0.76* (58.42*)	0.87* (17.83)	0.54* (1.25)	−0.22 (4.86)	−0.80* (0.11)

the Tropical Rainfall Measuring Mission (TRMM 3B43) were downloaded from the NASA Goddard Distributed Active Archive Center (DAAC) (http://trmm.gsfc.nasa.gov/) with a spatial resolution of 0.25° × 0.25° (~25 km at the equator). The precipitation of a lake was represented as the mean precipitation within its drainage basin. Temperature data were obtained from the China Meteorological Data Sharing Service System (http://data.cma.gov), and the data collected at the gauge station closest to each lake were used to represent its temperature conditions.

Apart from these natural drivers, nutrient loads, mostly from human perturbations, may be major contributors to phytoplankton growth (Marra et al., 1990) and Chla abundance in the water column. The nutrient inputs from three major sources, including chemical fertilizer consumption from surrounding counties, industrial sewage from lake-adjacent cities and livestock excrement from the lake drainage basin, were compiled to study the influence of human activities on lake eutrophication. Fertilizer consumption was obtained from the provincial statistical yearbook (Feng et al., 2019), and industrial sewage for each lake was obtained from the China City Statistical Yearbook (Feng et al., 2019; Liu et al., 2013). The amount of livestock excrement in the lake drainage (Q, in kg) basin was estimated as the total excreta from the major feeding animals, including cow, sheep, pig, fowl, and rabbit, in the middle and lower reaches of the Yangtze River basin, which can be expressed as:

$$Q = \sum_{i=1}^{n} c_i N_i T_i \tag{3}$$

where c_i is the excretory coefficient measuring the amount of excrement per day, which varies between different types of livestock and was adopted from Wei et al. (2016); N_i is the number of livestock raised in

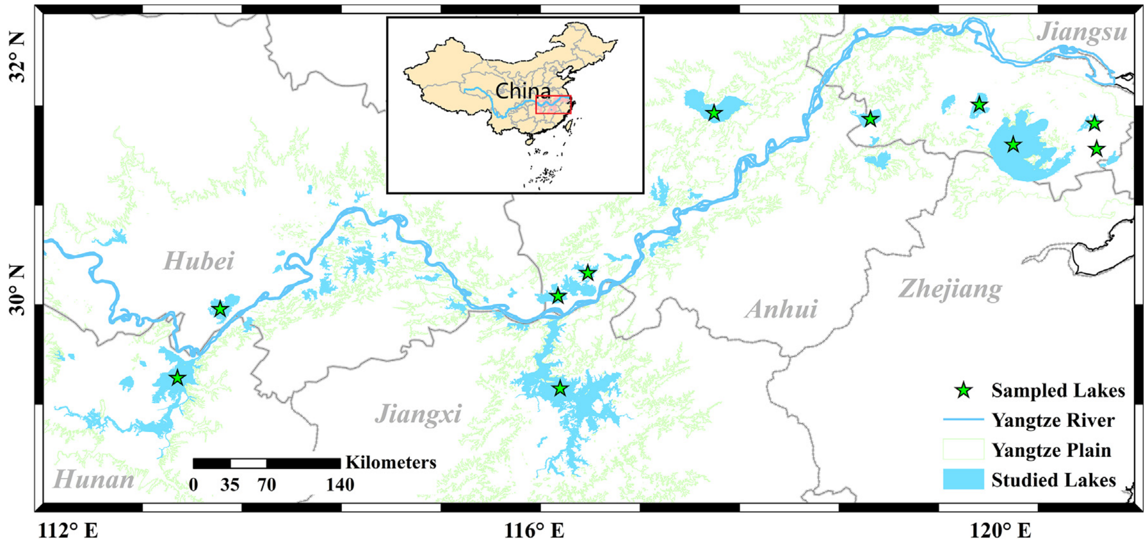

Fig. 1. Locations of the 50 examined lakes on the Yangtze Plain of China (red box in the inset). The green polygon represents the boundary of the Yangtze Plain, and the 11 sampled lakes are annotated with green stars. (For interpretation of the references to color in this figure legend, the reader is referred to the web version of this article.)

the drainage basin and was obtained from the provincial statistical yearbook; and T_i is the number of feeding days of livestock and was based on empirical data from Geng et al. (2013).

3. Methods

The floating algal bloom area (ABA) and Chla concentrations derived from the MERIS and OLCI observations were used to examine the eutrophic status of the Yangtze Plain lakes, and Chla estimations were only applied to bloom-free waters. Note that the algal bloom detected in the Yangtze Plain lakes in our study mainly represent floating cyanobacteria bloom, as documented in many previous studies (Duan et al., 2012; Hu et al., 2010; Ma et al., 2008; Qi et al., 2014b; Zhang et al., 2016; Zhu et al., 2017). The entire working flow is summarized in Fig. 3, and the detailed methods for each step are described below.

3.1. Generation of land mask and shallow water mask

The first step is to classify the water and land area in each remote sensing image. Based on the remarkable spectral differences, a commonly used spectral index, the normalized difference water index (NDWI, estimated as $(R_{rc,560} - R_{rc,865})/(R_{rc,560} + R_{rc,865})$, (Gao, 1996)), was used to distinguish water from land area. The optimal image-specific thresholds were determined through an interactive graphical user interface developed in Hou et al. (2017).

Some parts of lakes (or sub-lakes) on the Yangtze Plain showed shallow and/or clear waters, such as eastern Taihu Lake, southern Poyang Lake, and almost all of Honghu Lake. The reflection from the bottom, which is mostly covered by submerged vegetation (identified by field investigations), could contaminate the satellite signals and thus impact the retrieval of Chla concentrations (Kutser et al., 2020). Because shallow water with submerged vegetation results in low NDWI values similar to those obtained from vegetation-free waters, an additional mask was generated to exclude these optically shallow waters. When comparing the true color composite, we found that the areas with submerged vegetation (identified by field investigations) demonstrated large color contrasts to the other inundated regions (see Fig. S2). Therefore, a gray index (GI), estimated using the red, green and blue bands, was adopted to separate shallow waters. The GI was estimated as follows:

$$GI = R_{rs,681} \times 0.299 + R_{rs,560} \times 0.587 + R_{rs,443} \times 0.114 \quad (4)$$

The field-derived GI values for submerged vegetation-present and vegetation-free waters are plotted in Fig. S2, indicating that a simple threshold (GI = 0.01) could be used to effectively discriminate the two classes with high accuracy (86.8%), and we used this threshold to generate the mask for separating shallow waters from submerged plants. As submerged vegetation mainly blooms in spring, the images collected between March and May in each year were used to create annual masks for shallow water. Pixels that were identified as shallow water in any image acquired between March and May were excluded for further Chla estimation in the entire year.

3.2. Detection of the algal bloom area

The chlorophyll spectral index (CSI), based on the near-infrared (NIR) and red bands specifically designed for MERIS (Zhu et al., 2017), was used to distinguish cyanobacteria blooms from lake water, which could be expressed as:

$$CSI = \frac{R_{rc,754} - R_{rc,681}}{R_{rc,754} + R_{rc,681}} \quad (5)$$

where $R_{rc,754}$ and $R_{rc,681}$ are the Rayleigh-corrected reflectance values at 754 nm and 681 nm, respectively. The concept of the CSI is to make use of the significant signal contrasts between ABA and algae-free waters at the NIR band (i.e., 754 nm), where a strong reflection for floating algae and a high absorption for waters are expected. The threshold recommended by Zhu et al. (2017), CSI = 0.11, was used in this study to classify ABAs. The threshold was originally generated based on 52 MERIS images over Taihu Lake (Zhu et al., 2017), and a validation performed using in situ recorded datasets collected in the Yangtze lakes also demonstrated a high accuracy level of 88.9% for separating ABA and algae-free waters (see Fig. S2) with OLCI images. Note that although the widely used floating algae index (FAI) (Hu, 2009) is specifically designed for pelagic algae detection, the absence of a shortwave infrared band for MERIS and OLCI prohibited the application of FAI here.

High CSI values, which are normally associated with floating algae, can potentially originate from emergent vegetation or floating leaf vegetation as well, leading to a misinterpretation of the eutrophication status. To further eliminate such impacts, the phycocyanin baseline (PBL) (Zhu et al., 2017) was used to discriminate the algal bloom and the above-water vegetation. The calculation of PBL is expressed as follows:

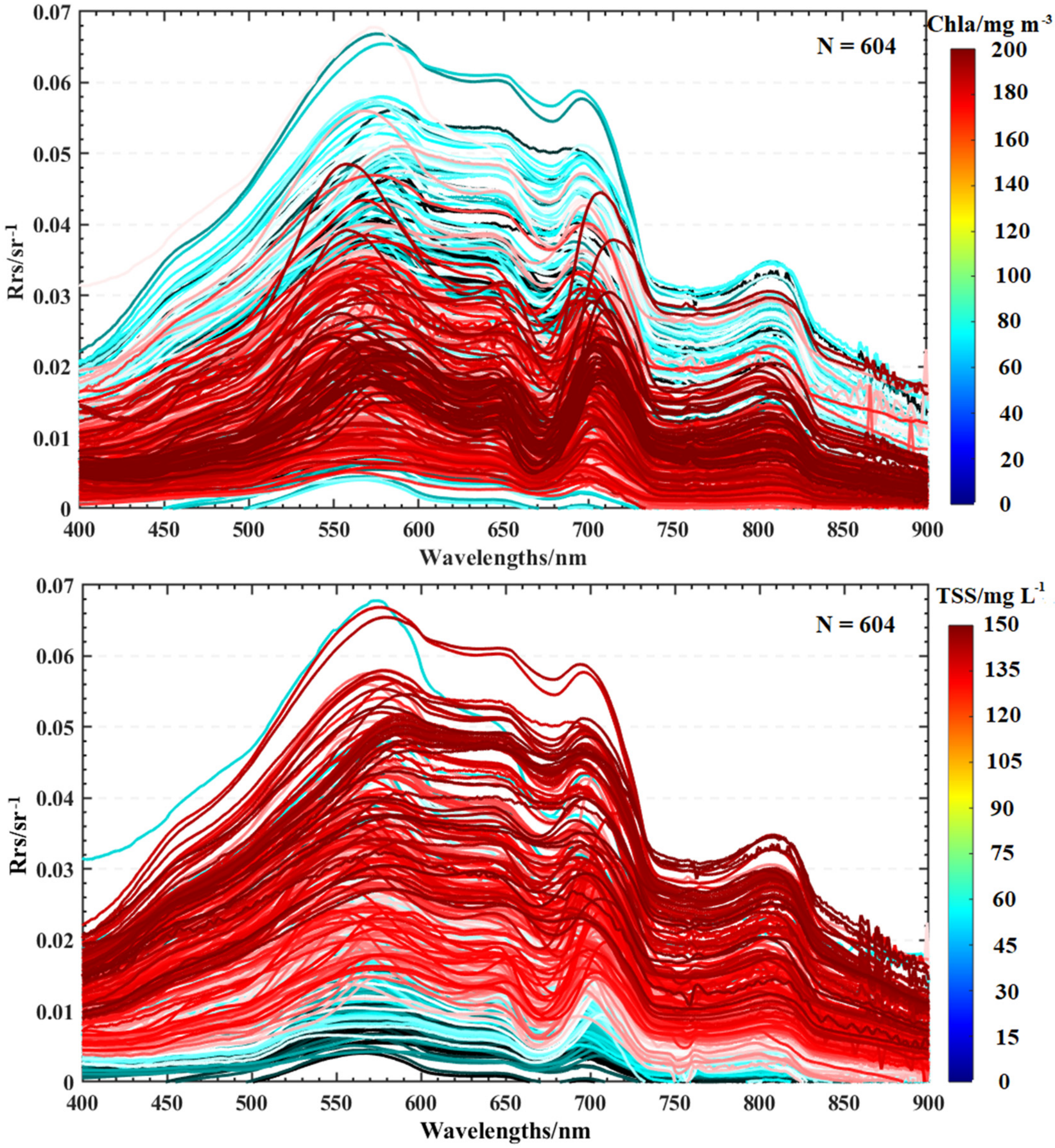

Fig. 2. Field-measured Rrs spectra color-coded according to their Chla (upper panel) and TSS (lower panel) concentrations.

Table 2
Statistical information about the measured concentrations of Chla and total suspended sediment (TSS) in the sampled lakes.

	Min	Max	Median	Average	STD	# of point
Chla, mg m^{-3}	1.16	222.57	15.56	22.21	27.62	604
TSS, mg L^{-1}	0.62	152.00	22.00	30.85	26.15	604

$$PBL = R_{rc,560} - R_{rc,620} + \left(\frac{620 - 560}{665 - 560}\right) \times (R_{rc,665} - R_{rc,560}) \quad (6)$$

The designation of the PBL is based on the unique curvatures of the spectrum for bloom areas, where two valleys near 625 nm and 675 nm could be clearly identified due to the strong absorption of phycocyanin and chlorophyll, respectively. These distinct spectral characteristics allow for an effective separation between cyanobacteria bloom and aquatic vegetation. In situ recorded datasets showed that the recommended threshold for the PBL (PBL = 0.009) by Zhu et al. (2017) led to an accuracy level of 77.6% (see Fig. S2). Although slightly smaller thresholds (such as 0) may result in higher accuracy levels in Fig. S2, a sensitivity analysis with smaller values showed almost identical long term Chla and ABA estimates (likely due to the additional mask dilation process, see below). Therefore, the recommended threshold (PBL = 0.009) was adopted in this study.

Before ABA delineation, a dilation process was applied to the above mentioned masks (including for land, shallow water and emergent vegetation) for each image to exclude one more pixel that is adjacent to the masks. Since these masking algorithms have already demonstrated satisfactory performances, the expanded mask could help us to avoid most of the problems associated with 300-m resolution induced mixing pixel problems for MERIS and OLCI. Then, quarterly and annual ABAs, estimated as the union areas of delineated algal blooms in all images within the corresponding period (i.e., a quarter or a year), could be interpreted as the maximum possible bloom area during this period. The use of maximum instead of mean values of bloom areas was chosen to minimize the impacts of clouds on quantified bloom conditions because the algal blooms were generally heterogeneously within a lake; thus, the ABA detected from partially cloud-covered images could not be used to represent the bloom conditions. The ABA of each lake was then normalized against lake size (see Table 1) to estimate the percentage of ABA, allowing for cross-lake comparisons despite the substantial disparities in lake sizes. The long-term changes in the quarterly and annual percentages of ABA were assessed for all the examined

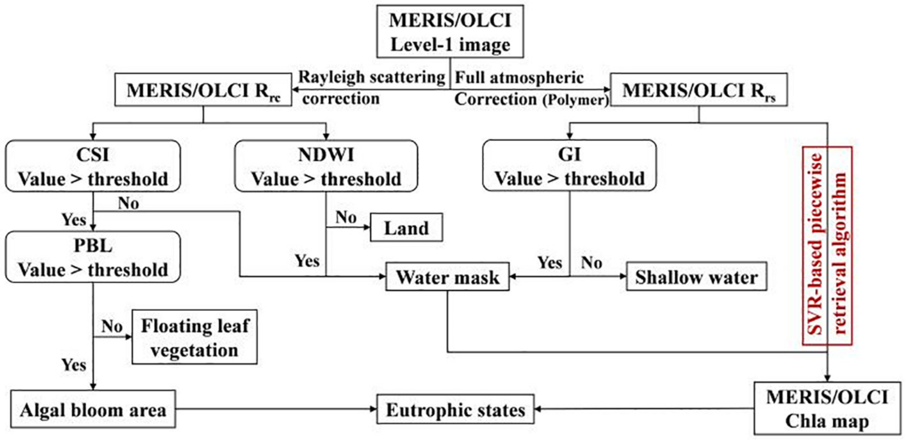

Fig. 3. Framework used to determine the lacustrine eutrophication state in this study. CSI, chlorophyll spectral index; NDWI, normalized difference water index; GI, gray index; and PBI, phycocyanin baseline.

lakes.

3.3. Development and validations of the Chla algorithm

A Chla algorithm was developed to determine the eutrophic conditions for bloom-free waters. Phytoplankton pigment dominates the absorption and scattering properties of open oceans, where blue-green band ratios were constructed for various ocean color missions to estimate the Chla concentrations (Hu et al., 2019; Hu et al., 2012; O'Reilly et al., 2000). These NASA-standard band ratio algorithms have recently been replaced with a band-difference approach (i.e., ocean color index or OCI), which is expected to significantly improve image quality and cross-sensor consistency. While the success of both the band ratio and the OCI algorithm relies on the high absorption feature of Chla in blue bands (Hu et al., 2019; Hu et al., 2012; O'Reilly et al., 2000), the signals of these short wavelengths are strongly affected by the presence of TSS and colored dissolved organic matter (CDOM) in inland and coastal waters. Therefore, longer wavelengths (red to NIR spectral regions) were selected to determine the Chla algorithm for these productive waters(Gilerson et al., 2010; Gitelson et al., 2008) to minimize the impacts of CDOM or sediment particles.

Various forms of combinations of MERIS/OLCI bands have been proposed to empirically correlate with in situ Chla concentrations (see Table 3), and the central wavelengths of these commonly used bands are 620-, 665-, 681-, 709- and 754-nm. Unfortunately, these existing retrieval algorithms exhibited poor performance (mean relative error (MRE) > 50%, root mean square error (RMSE) > 80%), even if the 604 field-collected pairs of spectra (i.e., MERIS/OLCI-equivalent bands) and Chla measurements from the Yangtze Plain lakes were used to recalibrate the algorithm coefficients (see Table 3). All these algorithms were well designed for inland or coastal waters, and their unsatisfactory performance was likely due to the higher turbidity of the lakes used in our study (TSS concentration reached > 100 mg L^{-1}, see Table 2) compared with the waters that were examined in previous studies. Therefore, a new retrieval algorithm was developed to accurately obtain the Chla concentrations of our studied waters (i.e., the Yangtze Plain lakes) using MERIS and OLCI observations.

While the combinations of NIR and red bands could not construct accurate empirical Chla algorithms, significant correlations were found between all these combinations and in situ Chla ($R^2 > 0.6$) (see Fig. S3). Support vector regression (SVR), a machine learning method, was then adopted to determine whether the NIR/red band combinations had a certain implicit nonlinear relationship with Chla. If so, then the SVR could better capture the observed variations in Chla. The detailed procedures used to establish a satisfactory algorithm are described below.

Linear correlations between all possible combinations (two or three bands) of the five red and NIR bands (620-, 665-, 681-, 709- and 754-nm) and in situ Chla were conducted. For correlation analysis, the normalized R_{rs} (denoted as R'_{rs}) values were used to minimize the first-order reflection signals from water turbidity (Feng et al., 2014b; Zhang et al., 2008a). The R'_{rs} for each band (λ_i) was estimated as the R_{rs} at this band normalized against the summation of MERIS and OLCI bands centered at 412-, 443-, 490-, 510-, 560-, 620-, 665-, 681-, 709-, 754- and 865-nm:

$$R'_{rs}(\lambda_i) = R_{rs}(\lambda_i) / \int_1^n R_{rs}(\lambda_i)d\lambda \tag{7}$$

The band combinations with high correlations were then selected as the inputs of SVR. To train and test the SVR model, the 604 R_{rs}-Chla pairs were randomly divided into two groups, where 495 pairs from 11

Table 3
Performance of different Chla retrieval algorithms, where the coefficients were recalibrated using the field-measured spectra and Chla datasets of the current study. Accuracy matrices for Chla estimates using both in situ (converted into satellite equivalent data using spectral response function for each band) and satellite Rrs are listed in the table.

Model	Order	Model inputs	Equation form	In situ-based			Satellite-based		
				MRE (%)	RMSE (%)	R^2	MRE (%)	RMSE (%)	R^2
Smith et al. (2018)	Piecewise	$x = R_{rs,709}/R_{rs,665}$ or Color Index (CI)	$y = (35.75*x\text{-}19.3)^{1.124}$ or $Chla_{OCI}$	50.54	82.13	0.60	66.12	88.26	0.23
Yang et al. (2010a)	NLR	$x = (R^{-1}_{rs,665} - R^{-1}_{rs,709})/(R^{-1}_{rs,754} - R^{-1}_{rs,709})$	$y = 79.855*x + 19.428$	63.93	114.63	0.67	57.01	83.85	0.16
Neil et al. (2019)	Power	$x = R_{rs,709}/R_{rs,665}$	$y = 16.409*x^{2.1313}$	58.00	93.50	0.60	50.00	65.35	0.05
Gurlin et al. (2011)	Poly (2d)	$x = (R^{-1}_{rs,681} - R^{-1}_{rs,709})R_{rs,754}$	$y = 77.199*x^2 + 107.51*x + 18.695$	66.81	119.33	0.70	67.54	98.97	0.15
Gurlin et al. (2011)	Poly (2d)	$x = R_{rs,709}/R_{rs,665}$	$y = 4.144*x^2 + 40.004*x\text{-}22.889$	64.96	104.27	0.62	57.60	78.73	0.22
Gilerson et al. (2010)	NLR	$x = R_{rs,709}/R_{rs,665}$	$y = 53.33*x\text{-}31.408$	64.41	101.27	0.62	72.56	92.75	0.02
Gitelson et al. (2008)	NLR	$x = (R^{-1}_{rs,681} - R^{-1}_{rs,709})R_{rs,754}$	$y = 145.88*x + 20.043$	59.53	101.40	0.69	54.38	80.44	0.18
SVR (this study)	Piecewise	Described in Section 3.3 and 4.1	–	25.67	35.46	0.93	26.92	33.13	0.55

lakes were used for training and the other 109 pairs from 8 lakes were used to validate the relationships. The kernel function for SVR was set as the radial basis function (RBF), and the grid iterative approach was employed to search the optimal penalty factor c and kernel function parameter δ to avoid under-fitting and overfitting problems (Su et al., 2015; Sun et al., 2009; Xiao et al., 2018). To evaluate the performance of SVR, the accuracy matrices were used based on the Chla estimates and field-measured samples, which include the MREs, RMSEs, unbiased relative mean-squared errors (URMSs), median ratio (MedR), mean ratio (MeanR) and coefficient of determination (R^2). After training and testing the SVR model, a reliable retrieval algorithm for Chla concentration at the basin scale was established.

The SVR algorithm based on in situ measurements was further validated through comparison between the satellite-derived and in situ Chla concentrations to assess its applicability for satellite observations (see Table 3). Atmospherically corrected MERIS and OLCI R_{rs} values were fed into the algorithm to estimate Chla concentrations for comparison with the concurrent in situ measurements. Several criteria were used to determine the satellite and in situ concurrent match-ups: first, the time differences between satellite overpassing and field sample collection was within 3-h to eliminate the effect of changes in the water conditions; second, a homogeneity test was applied to the satellite retrievals, discarding data with coefficients of variation (CVs) of the 3×3 window centered at the location of the field sampling > 15%; and third, areas with optically shallow waters within the 3×3 window (see detection method above) were removed. The same accuracy matrices were employed to assess the performance of the SVR-based retrieval algorithm on the MERIS and OLCI images. Note that, when determining the Chla concentrations, pixels associated with ABA regions and one additional pixel adjacent to ABA regions were removed to avoid potential mixtures between algae-free and bloom-occurred waters due to the 300-m resolution of the satellite images.

3.4. Assessments of the eutrophication status

To determine the chances of eutrophication for each lake, the annual probability of eutrophication occurrence (PEO) was estimated for all lakes: for both the MERIS and OLCI images, when a pixel had a Chla value > 10 mg m^{-3} (Shu, 1993) or was detected as an ABA, it was classified as a eutrophication region. The PEO (in percentage) was calculated as the number of times a pixel classified as an eutrophication region normalized against the number of valid satellite observations at the same location and within the same period (i.e., without contaminations with clouds and sun glint). Then, the mean PEO values were estimated for all lakes in the study period (see Table 1). Linear regression was then employed over the annual mean PEOs for each lake to explore the long-term trend of the lacustrine eutrophication status.

4. Results

4.1. Performance of SVR-based retrieval algorithm

After linear correlation analysis, six band combinations with high correlations ($R^2 > 0.60$), including $R'_{rs,709}/R'_{rs,620}$, $R'_{rs,709}/R'_{rs,665}$, $R'_{rs,709}/R'_{rs,681}$, $(R'_{rs,620}\text{-}R'_{rs,709})R'_{rs,754}$, $(R'_{rs,665}\text{-}R'_{rs,709})R'_{rs,754}$, and $(R'_{rs,681}\text{-}R'_{rs,709})R'_{rs,754}$ (relationships see Fig. S3), were selected as the inputs of the SVR model. The training and testing datasets were then used to train and test the SVR model, respectively. Comparisons between the estimated and field-measured Chla concentrations and the accuracy matrices are shown in Fig. 4 and Table 4, respectively. Although the accuracy matrices could vary between different lakes, similar overall uncertainty levels were found between the training and testing datasets, with an overall MRE of ~36%, an RMSE of ~60% and an URMS of ~40%, where the in situ and SVR-retrieved Chla were significantly correlated without apparent biases ($R^2 > 0.9$, MedR of ~1 and MeanR of ~1.15). Nevertheless, the scatter plots between the model-predicted and in situ-measured Chla demonstrated considerable uncertainty at low Chla values (see Fig. 4). Specifically, the uncertainty levels decreased with increasing Chla values until reaching Chla values higher than 10 mg m^{-3}. Therefore, further refinement of the SVR model was required to improve the performance at low Chla conditions.

The training samples with Chla < 10 mg m^{-3} were selected (141 pairs) to re-train an SVR model that is more suitable for low Chla concentrations. The correlations between the R'_{rs} and in situ Chla were reanalyzed, and significant correlations were then found between the log-transformed Chla and several band combinations. The band combinations included the band ratios of $R'_{rs,620}/R'_{rs,709}$, $R'_{rs,665}/R'_{rs,709}$ and $R'_{rs,681}/R'_{rs,709}$, and the spectral derivative of $(R'_{rs,709}\text{-}R'_{rs,620})/(709\text{–}620)$, $(R'_{rs,709}\text{-}R'_{rs,665})/(709\text{–}665)$, and $(R'_{rs,709}\text{-}R'_{rs,681})/(709\text{–}681)$ (see Fig. S4). The band combinations of these low Chla pairs were processed using the same method above to retrain the whole SVR model, with the expectation that the resulting algorithm (denoted as SVR-model$_{small}$) could derive more accurate Chla retrievals for low Chla conditions. Indeed, the validations from both the training and the testing datasets demonstrated substantial improvements for low Chla (i.e., < 10 mg m^{-3}) when the SVR-model$_{small}$ was used (see the solid points in Fig. 4), as demonstrated by the closer proximities of the points to the 1:1 line in Fig. 4. When the SVR model was used for high Chla and the SVR-model$_{small}$ was used for low Chla, both the training and the testing datasets showed improved estimations of the observed Chla matrices (i.e., overall MRE of < 25%, RMSE of < 36%, URMS of < 33%, MedR/MeanR close to 1 and $R^2 > 0.93$). Such accuracy levels appear comparable to the goal of ocean color satellite missions in obtaining Chla concentrations in global oceans (i.e., an uncertainty level of 35%) (Hu et al., 2012; O'Reilly et al., 2000).

From the above analysis, a piecewise Chla retrieval algorithm is proposed, with the SVR-model and SVR-model$_{small}$ applied for high and low Chla, respectively. In practice, a transition range (10–13 mg m^{-3}) instead of an absolute threshold (i.e., 10 mg m^{-3}) was used to assure smooth transitions between the two SVR models on Chla maps. The piecewise algorithm can be expressed as follows:

$$Chla' = \begin{cases} Chla_{high}, \; Chla_{high} > 13 \\ \alpha \times Chla_{high} + \beta \times Chla_{low}, \; 10 < Chla_{high} \le 13 \\ Chla_{low}, \; Chla_{high} \le 10 \end{cases}$$
$$\alpha = \log_{10}(Chla_{low})/\log_{10}(Chla_{low} + Chla_{high})$$
$$\beta = \log_{10}(Chla_{high})/\log_{10}(Chla_{low} + Chla_{high}) \quad (8)$$

The total numbers of the resulting concurrent match-ups between in situ observations and satellite data were 61 and 119 for MERIS and OLCI, respectively; MERIS data were only found in Taihu Lake, and OLCI match-ups were obtained from three lakes (Taihu Lake, Poyang Lake and Honghu Lake) because of unfavorable conditions (such as clouds and sun glint) during the satellite observations. The comparison of the satellite-based and in situ Chla is shown in Fig. 5. The plots of the predicted and measured Chla were generally distributed along the 1:1 line for both instruments and for all the lakes, and the associated accuracy statistics showed favorable performances (i.e., uncertainty levels < 40% without systematic biases). Satellite-based validations also showed smaller uncertainty levels of the SVR-based algorithm compared with the existing Chla algorithms (see Table 3). Considering the differences in spatial scales (300 × 300 m for MERIS and OLCI, and point-based observations for field sampling), the overall performance of the piecewise retrieval algorithm was considered acceptable. Therefore, the algorithm in Eq. (8) was used to derive the long-term Chla concentrations for the study lakes with MERIS and OLCI observations.

4.2. Long-term eutrophication change patterns in lakes on the Yangtze Plain

Eq. (8) was used to generate a Chla map for each MERIS and OLCI image. The averaged quarterly Chla was computed to represent the

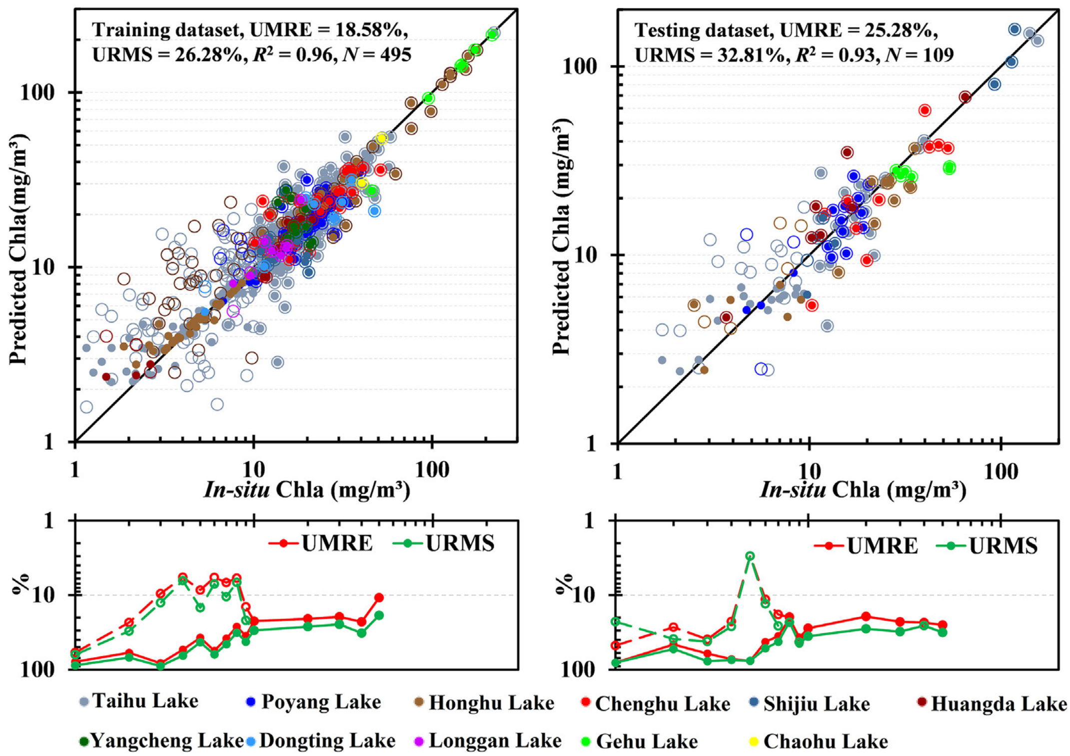

Fig. 4. Comparison between in situ measured Chla and SVR-estimated Chla for training (a) and testing (b) datasets. The solid points and colored circles indicate the Chla estimates with and without the refinement process for low Chla values (i.e., < 10 mg m^{-3}), respectively. The bottom panels present the unbiased mean relative error (UMRE, red lines) and unbiased relative mean-squared error (URMS, green lines) as a function of Chla for training (c) and testing (d) datasets. The dashed and solid lines indicate the results with and without the refinement process for low Chla values, respectively. (For interpretation of the references to color in this figure legend, the reader is referred to the web version of this article.)

quarterly mean values, where the four quarterly means were further averaged to estimate the annual mean Chla. The 11-year mean values of Chla were calculated from the annual mean values for both MERIS (2003–2011) and OLCI (2017–2018). Considerable differences were found in mean Chla among the examined lakes (Fig. 6a, Table 1), where the mean Chla concentration ranged from 17.58 mg m^{-3}(Taihu Lake) to 43.86 mg m^{-3}(Wushan Lake) in the Yangtze Plain. Generally, large Chla values occurred in small lakes (red colors in Fig. 6a), and large lakes were often found to have a low climatological mean Chla (blue colors in Fig. 6a). In terms of long-term trends, statistically significant increasing trends (i.e., $p < .05$) were found in 11 lakes, and statistically significant decreasing trends occurred in only 6 lakes (annotated with "↑" and "↓", respectively, in Fig. 6a). Spatially, the lakes with significant increasing trends were mainly located upstream of Poyang Lake, while lakes with statistically significant decreasing trends were mainly located within Jiangsu Province. The seasonality of the Chla distributions could be observed from the climatological quarterly mean Chla maps in Fig. 7. Most of the lakes demonstrated their largest Chla

Table 4
Performance of the SVR-based piecewise retrieval algorithm for individual lakes based on Chla estimated using field-measured spectra.

	Name	MRE/%	RMS/%	UMRE/%	URMS/%	MedR	MeanR	R^2	R^2 (Log)	N
Training dataset	Taihu	20.16	31.53	19.39	27.66	0.95	1.02	0.92	0.87	272
	Poyang	15.99	21.79	16.78	22.01	0.89	0.92	0.62	0.75	67
	Honghu	14.12	22.53	13.62	21.14	1.01	1.03	0.98	0.97	67
	Chenghu	26.61	36.29	24.38	29.99	0.95	1.06	0.66	0.59	24
	Shijiu	23.03	30.76	24.42	32.11	0.89	0.93	0.03	0.05	17
	Huangda	13.13	19.92	12.55	17.78	1.02	1.02	0.94	0.97	13
	Yangcheng	31.63	41.93	27.75	34.52	0.99	1.13	0.36	0.37	10
	Dongting	22.80	27.67	26.74	34.48	0.88	0.86	0.47	0.78	9
	Longgan	14.31	17.12	13.97	16.25	0.96	1.01	0.67	0.72	8
	Gehu	8.20	16.56	9.91	20.71	0.98	0.92	0.99	0.98	6
	Chaohu	14.79	17.79	17.10	20.36	0.91	0.91	N/A	N/A	2
	Overall	19.03	29.06	18.58	26.28	0.98	1.00	0.96	0.90	495
Testing dataset	Taihu	25.77	37.42	24.46	33.41	1.00	1.05	0.97	0.92	40
	Poyang	19.20	23.19	18.05	22.05	1.04	1.04	1.00	0.90	17
	Honghu	22.64	40.08	28.52	35.59	0.90	0.95	0.85	0.92	16
	Chenghu	30.17	33.33	33.00	38.00	0.83	0.91	0.68	0.73	10
	Shijiu	18.36	23.48	20.75	23.80	0.90	1.00	0.90	0.95	8
	Huangda	39.10	54.65	27.43	36.67	1.21	1.37	0.90	0.89	7
	Gehu	23.31	28.99	28.63	36.76	0.82	0.77	0.52	0.47	6
	Longgan	23.04	28.05	27.86	34.64	0.76	0.79	0.74	0.91	3
	Overall	25.67	35.46	25.28	32.81	0.95	1.01	0.93	0.88	109

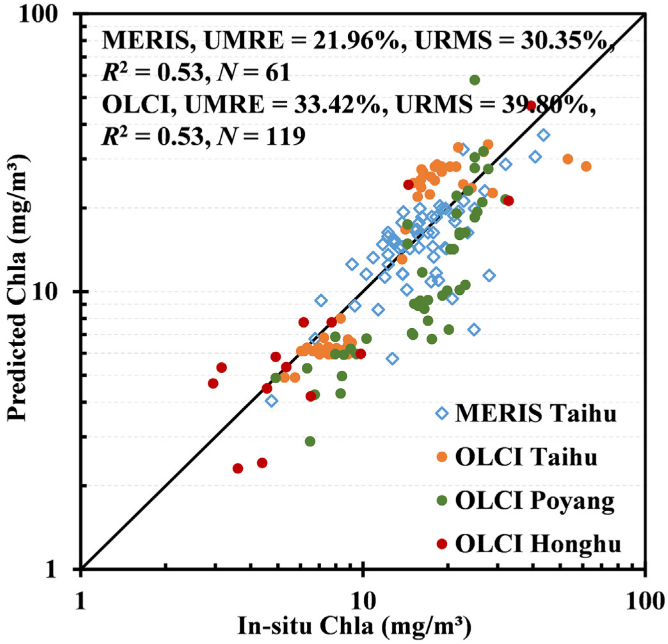

Fig. 5. Validation of the satellite-predicted Chla concentrations using in situ Chla data obtained from different lakes and satellite instruments. The accuracy measures estimated for both MERIS and OLCI are also annotated.

values in the second and third quarters of a year (see Fig. 7e), and cold seasons (especially quarter 1) often showed the lowest Chla within a year. While Chla seasonality could be observed across the panels, substantial spatial disparities in Chla within the larger lakes were also found.

Algal bloom detection was conducted for all 50 examined lakes at quarterly and annual timescales to determine the ABA percentage (Fig. 8). Similar to many other previous studies (Li et al., 2017; Zhang et al., 2016; Zhang et al., 2015), severe floating algal blooms were found in Taihu Lake and Chaohu Lake. The annual ABA of Chaohu Lake showed strong annual variability but significantly increased trend throughout the observational period. Likewise, an increasing trend was observed in Taihu Lake, e.g., the ABA was 6.95% (176 km^2) in 2003 but 75.25% (1909 km^2) in 2017. Seasonal variations were also present in the ABA percentage, where larger blooms generally occurred in warmer seasons, similar to the patterns observed in the Chla concentrations. In addition to the two previously known lakes with algal blooms, there were another five lakes on the Yangtze Plain that were found to have evidential algal blooms, including Beimin Lake, Huanggai Lake, Wanghu Lake, Tangxun Lake and Zhangdu Lake. Serious algal blooms occurred in Huanggai Lake in most of the observational years except for 2009 and 2011, and the bloom area reached > 85% in the two consecutive years of 2005 and 2006. Beimin Lake also showed large-scale algal blooms in several years, with an annual mean coverage > 67.5% of the lake area whenever the bloom occurred in that year. The first algal bloom of Wanghu Lake was found in 2008, and then blooms reoccurred in this lake in all subsequent years except 2009. Another important finding was that the algal blooms in Tangxun Lake and Zhangdu Lake were found only in the OLCI observation period, further indicating the strength of using multisource remote sensing observations. Notably, the annual algal bloom percentages demonstrated different fluctuation patterns from those of the PEOs for most of the 7 lakes.

The long-term mean PEO map is shown in Fig. 6b, where all of the lakes showed a mean value of > 50% (mostly > 80%), suggesting the extremely high probability of eutrophication for lakes on the Yangtze Plain. The highest mean PEO value (95.9%) was found in Gehu Lake, indicating that almost the entire observational period showed eutrophication (i.e., Chla > 10 mg m^{-3} or algal bloom detected) from the MERIS and OLCI observations. Similar to the patterns observed for Chla, large lakes tended to have lower PEOs than small lakes. The long-term interannual changes in the PEO for all 50 lakes were illustrated in Fig. 9. Although the annual mean PEO values fluctuated throughout the period, 21 out of 50 lakes (42%) demonstrated statistically significant decreasing trends in PEO (annotated in Fig. 6b and Fig. 9), while only Wanghu Lake showed statistically significant increasing trends in PEO (annotated in Fig. 6b and Fig. 9).

4.3. Analysis of potential driving forces

To further understand the impacts of the natural factors and human activities on the interannual variability of the eutrophication conditions, correlations between the annual mean PEO and the concurrent driving factors (i.e., temperature, precipitation, chemical fertilizer, industrial wastewater and biological excrement) for each lake were analyzed, and the correlation coefficients are listed in Table 1. The PEO of these examined lakes exhibited significant correlations with different driving factors, which indicated that the dynamics of eutrophication conditions were affected by different natural and anthropological factors. The PEO of many lakes was significantly correlated with more than one factor, suggesting the complexity of the controlling environments that affect phytoplankton growth. Indeed, 70% (35/50) of the studied lakes were statistically significantly correlated ($p < .05$) with at least one of the given five driving factors (see Table 1).

Specifically, statistically significant positive correlations ($p < .05$) were revealed between the annual mean PEO and the annual consumption of chemical fertilizer in 18 lakes (see Fig. S5), suggesting the remarkable detrimental impacts of agricultural nonpoint pollution sources in this region. Moreover, 12 of the lakes had PEO values that were positively correlated ($p < .05$) with the industrial wastewater (see Fig. S6), and 10 lakes had significant positive correlations ($p < .05$) between the PEO value and the amount of biological excrement surrounding the lake (see Fig. S7). In terms of natural factors, the annual mean PEO of 16 lakes showed significant negative correlations ($p < .05$) with the annual mean precipitation (see Fig. S8), and significant positive relationships ($p < .05$) between PEO and temperature were found in 5 lakes (see Fig. S9). Note that opposite relationships to the aforementioned correlations were also found between the PEO and these examined factors, while the number of lakes with such abnormal correlations were relatively limited (see Table 1). Indeed, when considering only the 21 lakes with a significant decreasing trend in PEO (see Fig. 6b), similar correlation patterns were found compared to the situations when all lakes were included, where the PEOs were significantly correlated with various factors without a dominant factor.

A multiple general linear model regression (Tao et al., 2015) was used to quantify the relative contributions of these natural and anthropological factors to the interannual changes in the PEO of each examined lake. As shown in Table 1, the total contributions of these five driving factors varied from 10.52% to 99.86%, with 42 of the lakes showing a total value of > 50%. The mean total contribution for the 50 lakes was 72.26% ± 20.49%, indicating that these five natural and anthropological factors explained substantial amounts of the interannual dynamics in PEO for most of the 50 lakes. Specifically, fertilizer use was highly correlated with the PEO in Wanghu Lake ($R^2 = 0.84$) (see Table 1), and the significant increase fertilizer use in this lake contributed to 69.73% of inter-annual changes of PEO, making Wanghu Lake the only lake that showed significantly increased PEO during the observed period (see Fig. 9). Nevertheless, we acknowledge that more sophisticated ecological models are required in the future to understand the physical mechanisms of the impacts of these factors, particularly in relation to the overall decreasing patterns of the PEO in recent years.

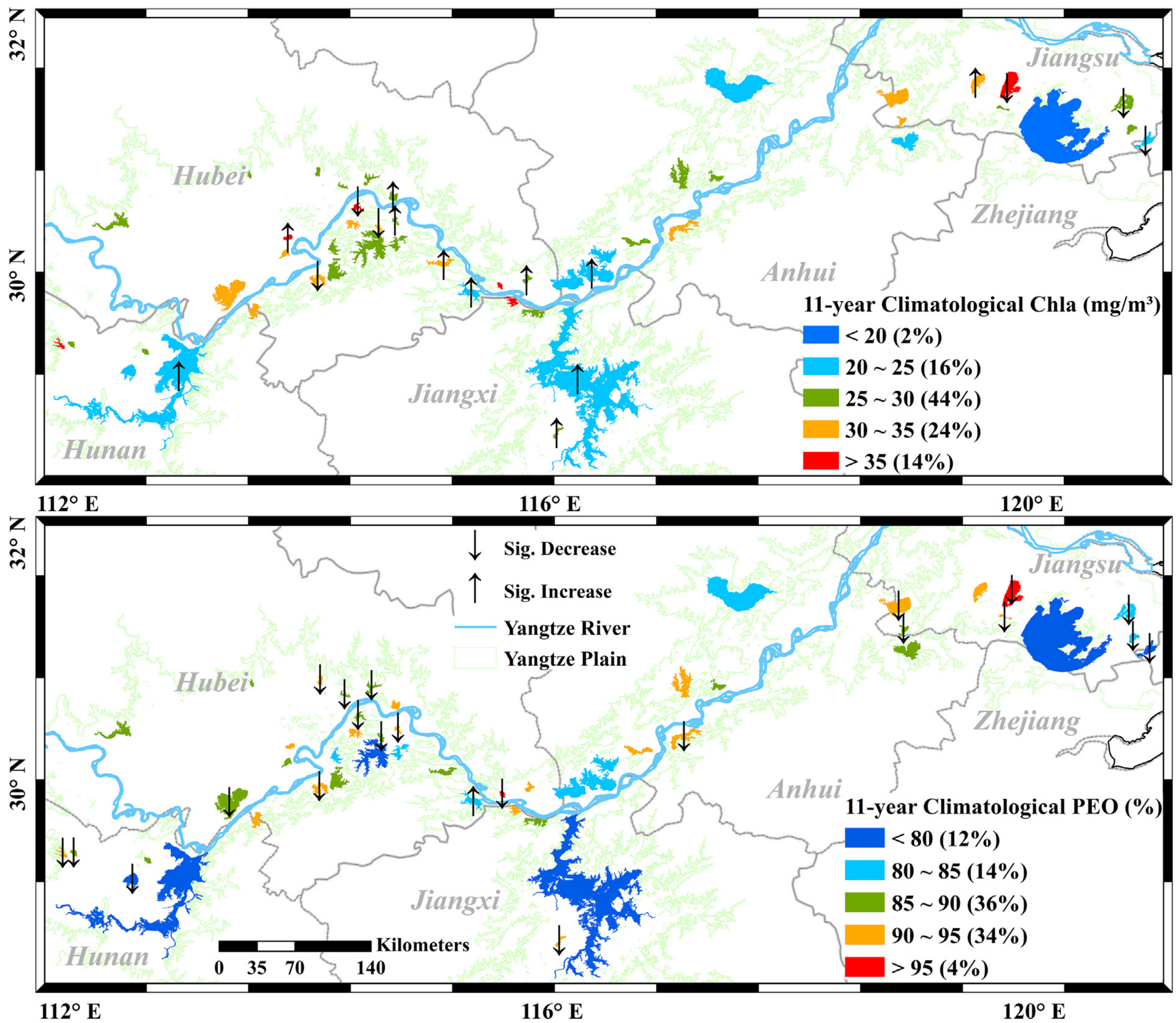

Fig. 6. Spatial distributions of climatological (a) Chla and (b) PEO for the 50 studied lakes on the Yangtze Plain (YP) from the MERIS and OLCI observations. The annotations "↑" and "↓" represent statistically significant increasing and decreasing trends, respectively, over the study period. The numbers in the parenthesis beside the legend are the number of lakes within the corresponding ranges.

5. Discussion

5.1. Uncertainties in the estimated eutrophication

Using the retrieved Chla and delineated ABA from the MERIS and OLCI images, the temporal and spatial changes in the eutrophication status for 50 large lakes on the Yangtze Plain have been documented, and obtaining such changes with traditional field sampling methods alone appears challenging. The accomplishments of the current study could primarily be attributed to the following reasons: 1) the availability of long-term MEIRIS and OLCI images, with adequate resolutions in the spectral and spatial domains and similar band configurations between the two instruments; and 2) sufficient field measurements from various lakes and across different seasons on the Yangtze Plain, which made it possible for us to develop and evaluate a machine-learning-based Chla algorithm. Nevertheless, there are still limitations in terms of quantifying the eutrophication status of lakes on the Yangtze Plain.

Although both MERIS and OLCI had a revisiting period of 2–3 days because of their wide swath (1150 and 1270 km, respectively), the number of usable images was limited due to the non-optimal observational conditions, which is a common problem for remote sensing-based optical observations. The global mean cloud coverage was estimated to be higher than 70% (King et al., 2013), which could substantially reduce the chance of obtaining high-quality optical remote sensing observations. Although the atmospheric correction method used in this study (POLYMER) has shown to be insensitive to sun glint and cloud straylight when compared with the classic approaches (Steinmetz et al., 2011; Steinmetz and Ramon, 2018; Zhang et al., 2018), the percentage of high-quality images was only ~17% of the entire data archive for the study area. Considerable data gaps could thus be found during the observational period, even with the entire dataset obtained from MERIS and OLCI, leading to potential uncertainties in the derived annual mean data and then the long-term trends. We tried to minimize such uncertainties through the currently used statistical schemes, where the annual mean Chla or ABA were estimated from the corresponding four quarterly mean values instead of the mean daily values within a year. Certainly, more frequent (daily or even hourly) satellite observations are recommended in the future to monitor the short-term to long-term variability of the dynamic water optical properties.

The POLYMER approach used here showed better performance than the SeaDAS embedded atmospheric correction algorithm (see Fig. S1). Nevertheless, previous studies has been previously reported that POLYMER may have larger uncertainties on blue bands than longer wavelengths (Zhang et al., 2018), while this issue has been largely circumvented in the current study, where the short wavelengths have already been excluded from Chla estimation to eliminate the signal

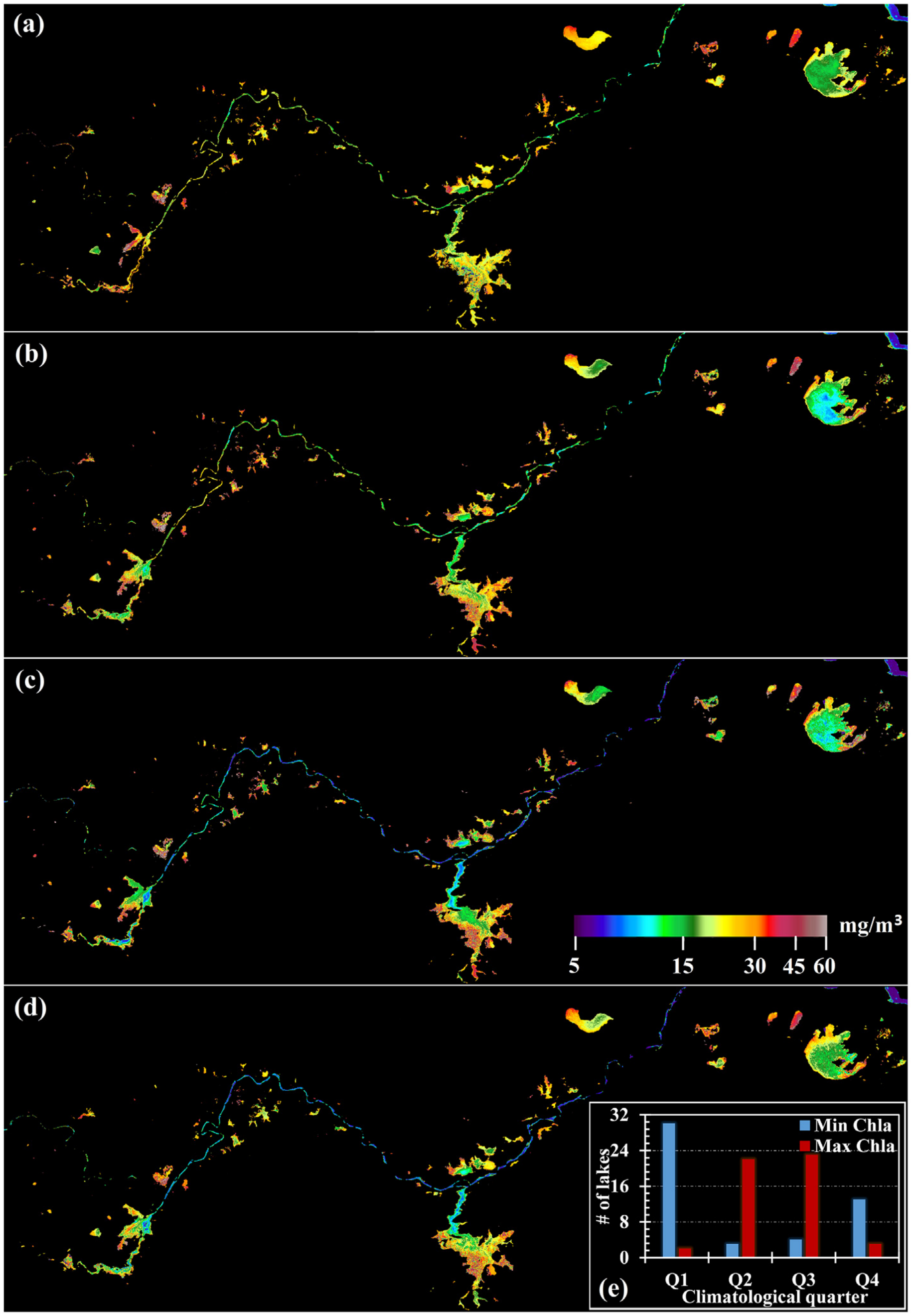

Fig. 7. The climatological quarterly-mean Chla distributions of the studied lakes (a-d represent from quarter 1 to quarter 4). (e) Histogram showing the number of lakes with minimum or maximum Chla occurring in different quarters (Q1 to Q4).

interventions from TSS and CDOM in inland and coastal waters. Furthermore, the exclusion of blue bands could minimize the residual errors from the bottom reflection, even after masking shallow water. This result is because short wavelengths often suffer from more severe contamination from bottom reflection due to their smaller water absorption coefficients and thus stronger penetration capability (Barnes et al., 2013; Lee et al., 1999; Mobley and Sundman, 2003). Nevertheless, future efforts are required to develop more advanced techniques to quantify the signals from shallow lake bottoms and allow for conducting Chla retrieval in the currently masked optically shallow waters.

The SVR algorithm was developed using the common bands (620-, 665-, 681-, 709-, 754-nm) available for both MERIS and OLCI, where the spectral ranges and band widths are highly consistent, making it possible to compare and quantify water quality changes using the data collected from these two instruments. However, the OLCI data are available only since 2017, approximately 5 years after MERIS stopped functioning. Although other satellite ocean color instruments (such as MODIS and VIIRS) have more continuous observations, they may be useful only for ABA detection and not for retrieving Chla on the Yangtze Plain because of the limited spectral information for these satellites, and/or they may be prone to saturation characteristics that prevent their capability to quantitatively retrieve Chla in the lakes on the Yangtze Plain. The gaps in the derived Chla between 2012 and 2016 for the Yangtze Plain lakes could also exist for many other similar water bodies in the world, which highlights the importance of continuous high-quality ocean color satellite measurements in the future.

The MERIS-derived PEO appeared to be lower than that from the OLCI for most of the lakes, and a possible systematic bias between these two instruments could also lead to such differences. Unfortunately,

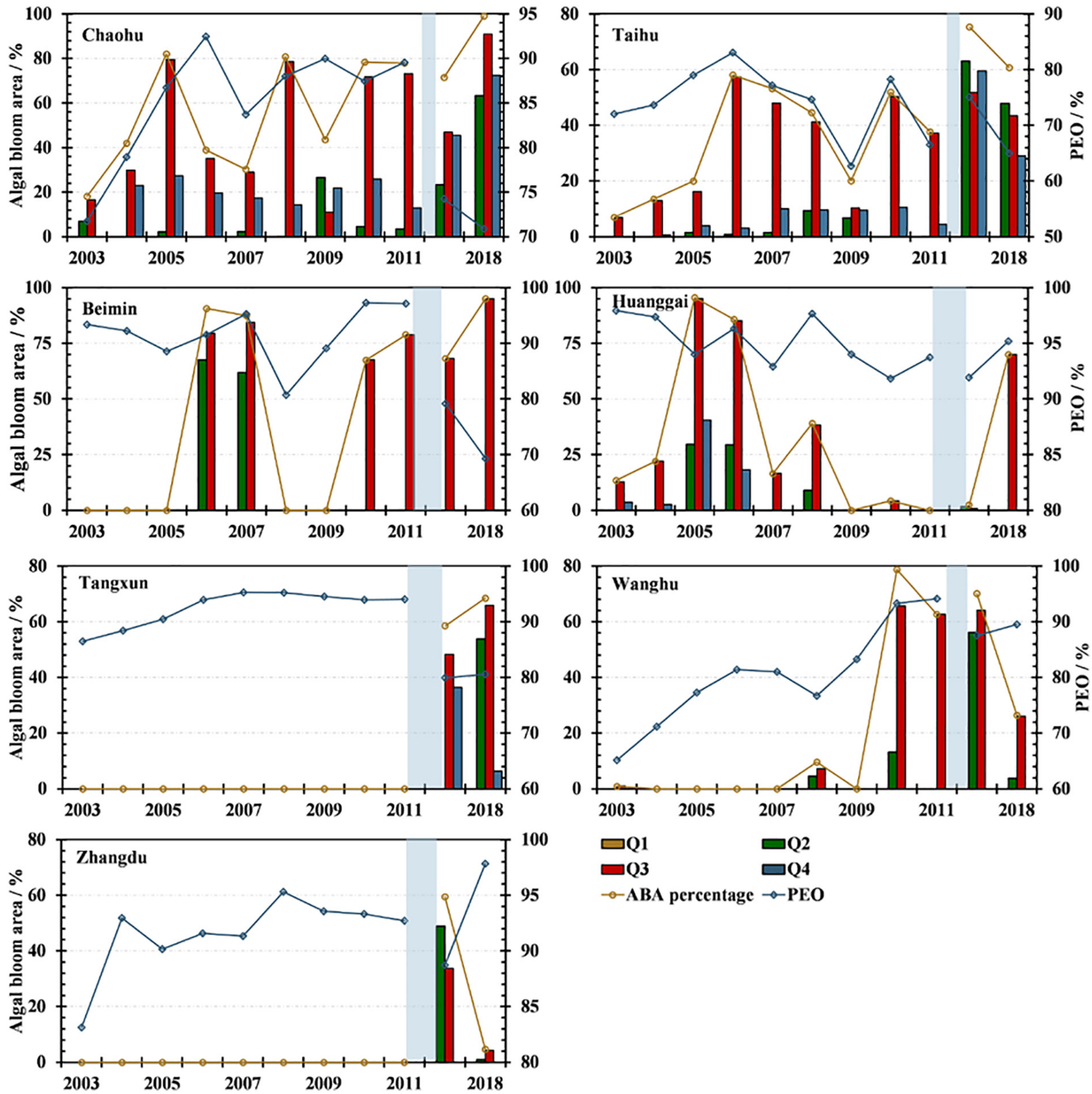

Fig. 8. Long-term changes in the quarterly and annual algal bloom area (ABA) percentage for 7 lakes where algal blooms were detected by MERIS and/or OLCI. The annual probability of eutrophication occurrence (PEO) for these lakes is also plotted. Shaded gray bar in each panel represents the observational gap between MERIS and OLCI.

direct comparison between these two types of observations is not possible due to the unavailability of concurrent observations. However, an alternative approach to determine the potential systematic bias between MERIS and OLCI could be the comparison of Chla concentrations derived from equivalent R_{rs} of MERIS and OLCI using field measurements. The spectral response functions of MERIS and OLCI were employed to compute the equivalent R_{rs}, which were then fed into the SVR-based Chla algorithm. When plotting the Chla retrievals for the two instruments (i.e., R_{rs} computed with different spectral response functions) against each other (see Fig. 10), a high consistency was found between MERIS and OLCI (R^2 = 0.99, slope = 1.03), indicating limited impacts of the cross-sensor differences on the long-term trends of lacustrine eutrophication conditions. Indeed, such high agreement was because the spectral bands used for Chla retrieval shared very similar band configurations (central wavelengths and band widths) between MERIS and OLCI. Furthermore, MERIS and OLCI share a number of other similarities, including field-of-view (68.5° for both), swath width (1150 km for MERIS and 1270 km for OLCI, respectively), and smile effects (1.7 nm for different cameras and 1.0 nm within one camera for MERIS and 1.4 nm for different cameras and 1.0 nm within one camera for OLCI) (D'Alba and Colagrande, 2005; Vicent et al., 2016; Zurita-Milla et al., 2010), further indicating that Chla estimates using MERIS and OLCI should present small difference. Slightly lower signal to noise ratios of MERIS relative to OLCI are also unlikely to cause substantial differences in the Chla estimates (Bulgarelli and Zibordi, 2018), particularly for the productive inland waters (and thus high reflective signal) that were examined in our study. Moreover, the validity of the results could be further justified based on the two reasons: First, the performance of the derived Chla algorithm was satisfactory with both observations; second, a systematic bias could not explain the diverged change patterns of the PEO between different lakes (see Fig. 9).

The relatively coarse spatial resolution (300 m) for MERIS and OLCI may also introduce some uncertainties to the ABA and Chla estimates,

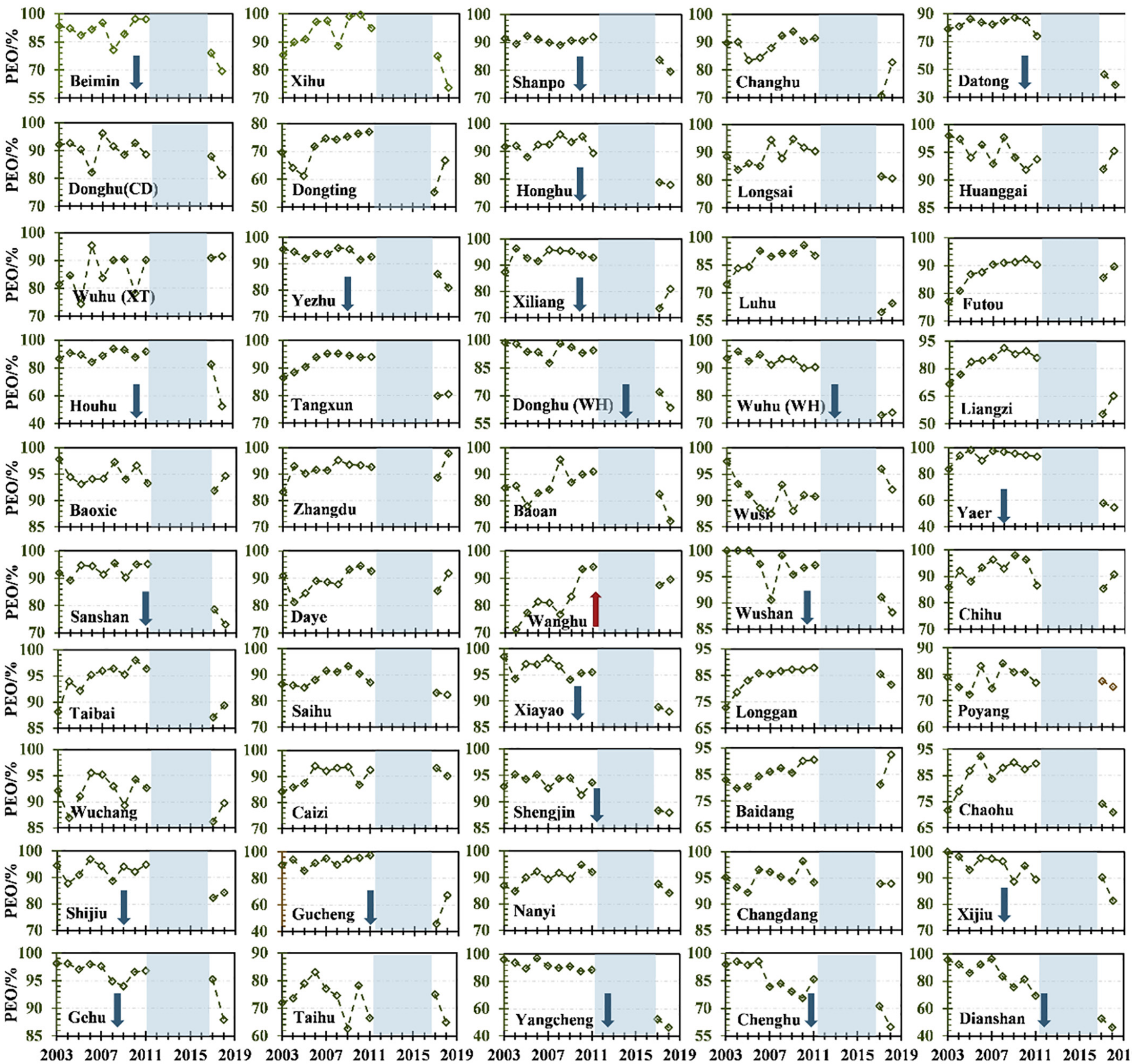

Fig. 9. The interannual changes in the mean PEO for each of the examined lakes on the Yangtze Plain observed from MERIS (2003 to 2011) and OLCI (2017 to 2018) observation periods, respectively. Lakes with statistically significant trends are annotated with arrows (blue and red represent decreasing and increasing trends, respectively). Shaded gray bar in each panel represents the observational gap between MERIS and OLCI. (For interpretation of the references to color in this figure legend, the reader is referred to the web version of this article.)

due to the heterogeneous nature of the aquatic environments (i.e., mixtures between algal bloom, shallow water, aquatic vegetation, etc.). Such impacts could be substantially reduced since we dilated one pixel over the masks determined for these perturbations. Nevertheless, even with 30 m spatial resolution and hyperspectal measurements (i.e., Hyperion), extremely small cyanobacterial blooms may be difficult to identify (Kutser et al., 2006). Therefore, advancements in satellite observations with higher resolution are required to minimize the mixing pixel associated problems.

5.2. Implications for lake ecosystems and society

Severe eutrophication can not only lead to cyanobacterial blooms that damage the aquatic ecosystem but also threaten public health by releasing toxic substances (i.e., microcystins) (Duan et al., 2014; Guo, 2007; Hu et al., 2010; Qin et al., 2007). Indeed, the lakes on the Yangtze Plain provide valuable water resources for surrounding cities or counties, which have more than 150 million people (numbers were estimated from (Wang, 2019; Xu and Wang (2017)). The quantified Chla concentration and the eutrophication status of 50 large lakes in this region can serve as baseline information for assessing the safety of drinking water resources (Duan et al., 2014; Xie et al., 2010). Moreover, the frequent OLCI observations for the entire globe are applicable to provide real-time and basin-scale monitoring of drinking water quality and potential risks once the currently developed methods are implemented as an operational mode.

Fishery aquaculture is extensively developed in the Yangtze Plain lakes to increase the incomes of the local residents and to meet the

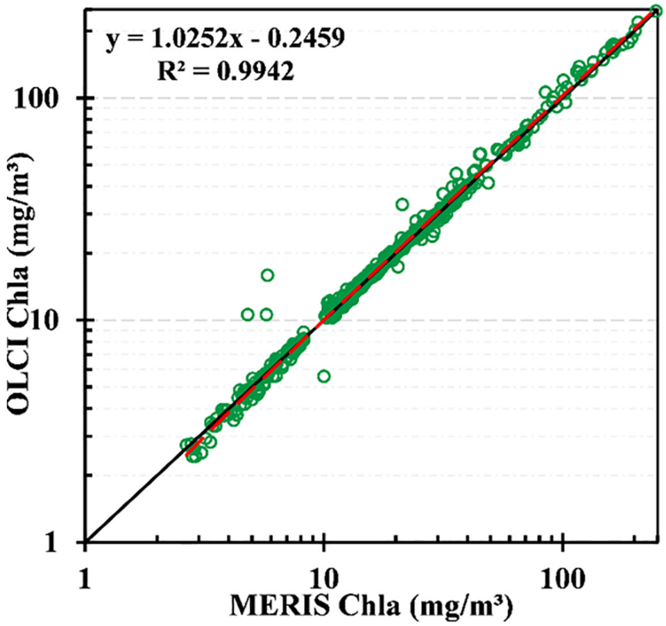

Fig. 10. Comparison of Chla concentrations derived with equivalent Rrs between MERIS and OLCI. The red dashed line is the fitting line. (For interpretation of the references to color in this figure legend, the reader is referred to the web version of this article.)

demand for protein food in the local region and in China (Chen et al., 2009; Hubacek et al., 2007; Poston and Duan, 2000); additionally, the production in the Yangtze Plain area accounts for ~60% of the total in the country (Fu et al., 2003). The aquaculture zones in the lakes are often separated from the main lake, by physical dikes or fishery nets. Such constructions could impact the circulation of water flow, potentially leading to less mixing and decomposing pollutants than that in natural water (Yuan et al., 2011). Furthermore, the use of bait, fertilizer and fishery drugs, with a direct loading of nutrients (e.g., nitrogen and phosphorus) into lakes, could significantly aggravate the eutrophication status in the lake water (Liu et al., 2013; Qin et al., 2007; Xu et al., 2010). To assess the impact of the fishery on the spatiotemporal dynamics of Chla and ABA, determining the exact locations of aquaculture is needed. Such a task appears to be challenging without continuous water quality estimates from large-scale satellite observations because the aquaculture activities are heterogeneously distributed in both the temporal and the spatial domains.

6. Conclusions

We proposed a SVR-based piecewise algorithm to accurately retrieve the Chla concentrations of 50 lakes on the Yangtze Plain using MERIS and OLCI images. The Chla estimates, together with satellite delineated ABAs, were used to determine the eutrophication status of the lake waters. All 50 examined large lakes showed high probabilities of eutrophication, with a climatological mean PEO > 50% (mostly > 80%). The PEO demonstrated statistically significant decreasing trends in 21 of the studied lakes for the period of the MERIS and OLCI observations, indicating the recent alleviation of eutrophication problems. To our knowledge, this study is the first attempt to comprehensively assess the eutrophication dynamics of basin-scale lakes on the entire Yangtze Plain. The SVR-based framework established in this study, explicitly developed for working with lakes with large variability of eutrophication levels, could be transferred to other regions and potentially to other inland and coastal environments for tracing long-term dynamics of water quality based on other satellite observations.

Author contributions

L.F. conceptualized the project, Q.G. processed the data and wrote an initial draft of the manuscript, and X.H. engaged in the field surveys and performed data analysis. All authors participated in interpreting the results and revising the manuscript.

Declaration of Competing Interest

None.

Acknowledgements

This work was supported by the National Key R&D program of China (NO: 2016YFC0402806), the National Natural Science Foundation of China (NOs: 41971304, 41671338, 41890852 and 41890851), the High-level Special Funding of the Southern University of Science and Technology (Grant No. G02296302, G02296402), and the State Environmental Protection Key Laboratory of Integrated Surface Water-Groundwater Pollution Control. We thank to Professor Liqiao Tian of Wuhan University, Guangzhou Water Color Ocean Technology Co., Ltd and Easy Ocean Technology Ltd. for their help in field instrument installment and integration. We also thank US NASA and ESA for providing MERIS and OLCI data, NASA for providing TRMM data, and the China Meteorological Data Sharing Service System for providing meteorological measurements. Two anonymous reviewers provided valuable comments to help improve this manuscript, whose effort is also appreciated.

Appendix A. Supplementary data

Supplementary data to this article can be found online at https://doi.org/10.1016/j.rse.2020.111890.

References

Barnes, B.B., Hu, C., Schaeffer, B.A., Lee, Z., Palandro, D.A., Lehrter, J.C., 2013. MODIS-derived spatiotemporal water clarity patterns in optically shallow Florida Keys waters: A new approach to remove bottom contamination. Remote Sens. Environ. 134, 377–391.

Bulgarelli, B., Zibordi, G., 2018. On the detectability of adjacency effects in ocean color remote sensing of mid-latitude coastal environments by SeaWiFS, MODIS-A, MERIS, OLCI, OLI and MSI. Remote Sens. Environ. 209, 423–438.

Chen, D., Xiong, F., Wang, K., Chang, Y., 2009. Status of research on Yangtze fish biology and fisheries. Environ. Biol. Fish 85, 337–357.

Cox, C., Munk, W., 1954. Measurement of the roughness of the sea surface from photographs of the sun's glitter. J. Opt. Soc. Am. 44, 838–850.

D'Alba, L., Colagrande, P., 2005. MERIS Smile Effect Characterization and Correction. Tech. rep ESA.

Du, Y., Xue, H.P., Wu, S.J., Ling, F., Xiao, F., Wei, X.H., 2011. Lake area changes in the middle Yangtze region of China over the 20th century. J. Environ. Manag. 92, 1248–1255.

Duan, H., Ma, R., Xu, X., Kong, F., Zhang, S., Kong, W., Hao, J., Shang, L., 2009. Two-decade reconstruction of algal blooms in China's Lake Taihu. Environ. Sci. Technol. 43, 3522–3528.

Duan, H., Ma, R., Hu, C., 2012. Evaluation of remote sensing algorithms for cyano-bacterial pigment retrievals during spring bloom formation in several lakes of East China. Remote Sens. Environ. 126, 126–135.

Duan, H., Loiselle, S.A., Zhu, L., Feng, L., Zhang, Y., Ma, R., 2014. Distribution and incidence of algal blooms in Lake Taihu. Aquat. Sci. 77, 9–16.

Fang, J., Rao, S., Zhao, S., 2005. Human-induced long-term changes in the lakes of the Jianghan Plain, Central Yangtze. Front. Ecol. Environ. 3, 186–192.

Fang, J., Wang, Z., Zhao, S., Li, Y., Tang, Z., Yu, D., Ni, L., Liu, H., Xie, P., Da, L.J.F.i.E., Environment, t., 2006. Biodiversity changes in the lakes of the Central Yangtze. 4. pp. 369–377.

Feng, L., Hu, C., Chen, X., Cai, X., Tian, L., Gan, W., 2012a. Assessment of inundation changes of Poyang Lake using MODIS observations between 2000 and 2010. Remote Sens. Environ. 121, 80–92.

Feng, L., Hu, C., Chen, X., Tian, L., Chen, L., 2012b. Human induced turbidity changes in Poyang Lake between 2000 and 2010: Observations from MODIS. J. Geophys. Res. Oceans 117.

Feng, L., Hu, C., Chen, X., Zhao, X., 2013. Dramatic inundation changes of China's two largest freshwater lakes linked to the Three Gorges Dam. Environ. Sci. Technol. 47, 9628–9634.

Feng, L., Hu, C., Chen, X., Song, Q., 2014a. Influence of the Three Gorges Dam on total suspended matters in the Yangtze Estuary and its adjacent coastal waters: Observations from MODIS. Remote Sens. Environ. 140, 779–788.

Feng, L., Hu, C., Han, X., Chen, X., Lin, Q., 2014b. Long-term distribution patterns of chlorophyll-a concentration in China's largest freshwater Lake: MERIS full-resolution observations with a practical approach. Remote Sens. 7, 275–299.

Feng, L., Han, X., Hu, C., Chen, X., 2016. Four decades of wetland changes of the largest freshwater lake in China: Possible linkage to the Three Gorges Dam? Remote Sens. Environ. 176, 43–55.

Feng, L., Hou, X., Zheng, Y., 2019. Monitoring and understanding the water transparency changes of fifty large lakes on the Yangtze Plain based on long-term MODIS observations. Remote Sens. Environ. 221, 675–686.

Fu, C., Wu, J., Chen, J., Wu, Q., Lei, G., 2003. Freshwater fish biodiversity in the Yangtze River basin of China: patterns, threats and conservation. Biodivers. Conserv. 12, 1649–1685.

Gao, B.-C., 1996. NDWI—A normalized difference water index for remote sensing of vegetation liquid water from space. Remote Sens. Environ. 58, 257–266.

Garcia, V.M.T., Signorini, S., Garcia, C.A.E., Mcclain, C.R., 2006. Empirical and semi-analytical chlorophyll algorithms in the south-western Atlantic coastal region (25–40°S and 60–45°W). Int. J. Remote Sens. 27, 1539–1562.

Geng, W., Hu, L., Cui, J., Bu, M., Zhang, B., 2013. Biogas energy potential for livestock manure and gross control of animal feeding in region level of China. Trans. Chin. Soc. Agric. Eng. 29, 171–179.

Gilerson, A.A., Gitelson, A.A., Jing, Z., Daniela, G., Wesley, M., Ioannis, I., Ahmed, S.A., 2010. Algorithms for remote estimation of chlorophyll-a in coastal and inland waters using red and near infrared bands. Opt. Express 18, 24109.

Gitelson, A.A., Dall'Olmo, G., Moses, W., Rundquist, D.C., Barrow, T., Fisher, T.R., Gurlin, D., Holz, J., 2008. A simple semi-analytical model for remote estimation of chlorophyll-a in turbid waters: Validation. Remote Sens. Environ. 112, 3582–3593.

Gong, J., Wu, G., Zhu, Q., de Leeuw, J., Skidmore, A.K., Liu, Y., Wang, S., Prins, H.H.T., Liu, Y., 2005. Exploring the possibility of estimating the aboveground biomass of *Vallisneria spiralis* L. using Landsat TM image in Dahuchi, Jiangxi Province, China. 6045. pp. 60452.

Gordon, H.R., Wang, M., 1994. Retrieval of water-leaving radiance and aerosol optical thickness over the oceans with SeaWiFS: a preliminary algorithm. Appl. Opt. 33, 443–452.

Guan, Q., Feng, L., Kuang, X., 2018. Optical classifications of Poyang Lake water and long-term dynamics based on MERIS observations. IEEE J. Select. Topics Appl. Earth Observ. Remote Sens. 1–13.

Guo, L., 2007. Ecology. Doing battle with the green monster of Taihu Lake. Science 317, 1166.

Gurlin, D., Gitelson, A.A., Moses, W.J., 2011. Remote estimation of chl-a concentration in turbid productive waters — Return to a simple two-band NIR-red model? Remote Sens. Environ. 115, 3479–3490.

Han, X., Chen, X., Lian, F., 2015. Four decades of winter wetland changes in Poyang Lake based on Landsat observations between 1973 and 2013. Remote Sens. Environ. 156, 426–437.

Hou, X., Feng, L., Duan, H., Chen, X., Sun, D., Shi, K., 2017. Fifteen-year monitoring of the turbidity dynamics in large lakes and reservoirs in the middle and lower basin of the Yangtze River, China. Remote Sens. Environ. 190, 107–121.

Hu, C., 2009. A novel ocean color index to detect floating algae in the global oceans. Remote Sens. Environ. 113, 2118–2129.

Hu, C., Lee, Z., Ma, R., Yu, K., Li, D., Shang, S., 2010. Moderate Resolution Imaging Spectroradiometer (MODIS) observations of cyanobacteria blooms in Taihu Lake, China. J. Geophys. Res. 115.

Hu, C., Lee, Z., Franz, B., 2012. Chlorophyll a algorithms for oligotrophic oceans: A novel approach based on three-band reflectance difference. J. Geophys. Res. Oceans 117.

Hu, C., Feng, L., Lee, Z., Franz, B.A., Bailey, S.W., Werdell, P.J., Proctor, C.W., 2019. Improving satellite global chlorophyll-a data products through algorithm refinement and data recovery. J. Geophys. Res. Oceans 124, 1524–1543.

Huang, L., Li, J., 2016. Status of freshwater fish biodiversity in the Yangtze River Basin, China. In: Aquatic Biodiversity Conservation and Ecosystem Services. Springer, pp. 13–30.

Hubacek, K., Guan, D., Barua, A., 2007. Changing lifestyles and consumption patterns in developing countries: A scenario analysis for China and India. Futures 39, 1084–1096.

Jiang, G., Loiselle, S.A., Yang, D., Ma, R., Su, W., Gao, C., 2020. Remote estimation of chlorophyll a concentrations over a wide range of optical conditions based on water classification from VIIRS observations. Remote Sens. Environ. 241, 111735.

King, M.D., Platnick, S., Menzel, W.P., Ackerman, S.A., Hubanks, P.A., 2013. Spatial and temporal distribution of clouds observed by MODIS onboard the Terra and Aqua satellites. IEEE Trans. Geosci. Remote Sens. 51, 3826–3852.

Kutser, T., Metsamaa, L., Strömbeck, N., Vahtmäe, E., 2006. Monitoring cyanobacterial blooms by satellite remote sensing. Estuar. Coast. Shelf Sci. 67, 303–312.

Kutser, T., Hedley, J., Giardino, C., Roelfsema, C., Brando, V.E., 2020. Remote sensing of shallow waters – a 50 year retrospective and future directions. Remote Sens. Environ. 240, 111619.

Le, C., Li, Y., Yong, Z., Sun, D., Huang, C., Lu, H., 2009. A four-band semi-analytical model for estimating chlorophyll a in highly turbid lakes: The case of Taihu Lake, China. Remote Sens. Environ. 113, 1175–1182.

Le, C., Zha, Y., Li, Y., Sun, D., Lu, H., Yin, B., 2010. Eutrophication of lake waters in China: Cost, causes, and control. Environ. Manag. 45, 662–668.

Le, C.F., Li, Y.M., Zha, Y., Sun, D.Y., Huang, C.C., Zhang, H., 2011. Remote estimation of chlorophyll a in optically complex waters based on optical classification. Remote Sens. Environ. 115, 725–737.

Lee, Z., Carder, K.L., Mobley, C.D., Steward, R.G., Patch, J.S., 1999. Hyperspectral remote sensing for shallow waters. 2. Deriving bottom depths and water properties by optimization. Appl. Opt. 38, 3831–3843.

Lee, Z., Ahn, Y.-H., Mobley, C., Arnone, R., 2010. Removal of surface-reflected light for the measurement of remote-sensing reflectance from an above-surface platform. Opt. Express 18, 26313–26324.

Li, J., Zhang, Y., Ma, R., Duan, H., Liang, Q., 2017. Satellite-based estimation of column-integrated algal biomass in nonalgae bloom conditions: a case study of Lake Chaohu, China. IEEE J. Select. Topics Appl. Earth Observ. Remote Sens. 10, 450–462.

Liu, B., Liu, H., Zhang, B., Bi, J., 2013. Modeling nutrient release in the Tai Lake Basin of China: Source identification and policy implications. Environ. Manag. 51, 724–737.

Liu, G., Simis, S.G.H., Li, L., Wang, Q., Li, Y., Song, K., Lyu, H., Zheng, Z., Shi, K., 2018. A four-band semi-analytical model for estimating phycocyanin in inland waters from simulated MERIS and OLCI data. IEEE Trans. Geosci. Remote Sens. 56, 1374–1385.

Liu, G., Li, L., Song, K., Li, Y., Lyu, H., Wen, Z., Fang, C., Bi, S., Sun, X., Wang, Z., Cao, Z., Shang, Y., Yu, G., Zheng, Z., Huang, C., Xu, Y., Shi, K., 2020. An OLCI-based algorithm for semi-empirically partitioning absorption coefficient and estimating chlorophyll a concentration in various turbid case-2 waters. Remote Sens. Environ. 239, 111648.

Luo, Q., Luo, L., Zhou, Q., Song, Y., 2019. Does China's Yangtze River Economic Belt policy impact on local ecosystem services? Sci. Total Environ. 676, 231–241.

Ma, R., Duan, H., Gu, X., Zhang, S., 2008. Detecting aquatic vegetation changes in Taihu Lake, China using multi-temporal satellite imagery. Sensors 8, 3988–4005.

Ma, R., Duan, H., Hu, C., Feng, X., Li, A., Ju, W., Jiang, J., Yang, G., 2010a. A half-century of changes in China's lakes: Global warming or human influence? Geophys. Res. Lett. 37.

Ma, R., Yang, G., Duan, H., Jiang, J., Wang, S., Feng, X., Li, A., Kong, F., Xue, B., Wu, J., Li, S., 2010b. China's lakes at present: Number, area and spatial distribution. Sci. China Earth Sci. 54, 283–289.

Marra, J., Bidigare, R.R., Dickey, T.D., 1990. Nutrients and mixing, chlorophyll and phytoplankton growth. Deep Sea Res. Part A. Oceanogr. Res. Pap. 37, 127–143.

Min, T., Duan, H., Cao, Z., Loiselle, S.A., Ma, R., 2017. A hybrid EOF algorithm to improve MODIS cyanobacteria phycocyanin data quality in a highly turbid lake: Bloom and nonbloom condition. IEEE J. Select. Topics Appl. Earth Observ. Remote Sens. 1–15.

Mobley, C.D., 1999. Estimation of the remote-sensing reflectance from above-surface measurements. Appl. Opt. 38, 7442–7455.

Mobley, C.D., Sundman, L.K., 2003. Effects of optically shallow bottoms on upwelling radiances: Inhomogeneous and sloping bottoms. Limnol. Oceanogr. 48, 329–336.

Mobley, C.D., Zhang, H., Voss, K.J., 2003. Effects of optically shallow bottoms on upwelling radiances: Bidirectional reflectance distribution function effects. Limnol. Oceanogr. 48, 337–345.

Mograne, M.A., Jamet, C., Loisel, H., Vantrepotte, V., Mériaux, X., Cauvin, A., 2019. Evaluation of five atmospheric correction algorithms over French optically-complex waters for the sentinel-3A OLCI Ocean Color Sensor. Remote Sens. 11, 668.

Müller, D., Krasemann, H., Brewin, R.J., Brockmann, C., Deschamps, P.-Y., Doerffer, R., Fomferra, N., Franz, B.A., Grant, M.G., Groom, S.B., 2015. The ocean colour climate change initiative: I. A methodology for assessing atmospheric correction processors based on in-situ measurements. Remote Sens. Environ. 162, 242–256.

Nakayama, T., Shankman, D., 2013. Impact of the Three-Gorges Dam and water transfer project on Changjiang floods. Glob. Planet. Chang. 100, 38–50.

Neil, C., Spyrakos, E., Hunter, P.D., Tyler, A.N., 2019. A global approach for chlorophyll-a retrieval across optically complex inland waters based on optical water types. Remote Sens. Environ. 229, 159–178.

Odermatt, D., Giardino, C., Heege, T., 2010. Chlorophyll retrieval with MERIS case-2-regional in perialpine lakes. Remote Sens. Environ. 114, 607–617.

O'Reilly, J.E., Maritorena, S., Siegel, D.A., O'Brien, M.C., Toole, D., Mitchell, B.G., Kahru, M., Chavez, F.P., Strutton, P., Cota, G.F., 2000. Ocean color chlorophyll a algorithms for SeaWiFS, OC2, and OC4: Version 4. In: SeaWiFS postlaunch calibration and validation analyses, Part, 3, pp. 9–23.

Pahlevan, N., Smith, B., Schalles, J., Binding, C., Cao, Z., Ma, R., Alikas, K., Kangro, K., Gurlin, D., Hà, N., Matsushita, B., Moses, W., Greb, S., Lehmann, M.K., Ondrusek, M., Oppelt, N., Stumpf, R., 2020. Seamless retrievals of chlorophyll-a from Sentinel-2 (MSI) and Sentinel-3 (OLCI) in inland and coastal waters: A machine-learning approach. Remote Sens. Environ. 240, 111604.

Pereira-Sandoval, M., Ruescas, A., Urrego, P., Ruiz-Verdú, A., Delegido, J., Tenjo, C., Soria-Perpinyà, X., Vicente, E., Soria, J., Moreno, J., 2019. Evaluation of atmospheric correction algorithms over Spanish inland waters for sentinel-2 multi spectral imagery data. Remote Sens. 11, 1469.

Poston, D.L., Duan, C.C., 2000. The current and projected distribution of the elderly and eldercare in the People's Republic of China. J. Fam. Issues 21, 714–732.

Qi, L., Hu, C., Duan, H., Barnes, B., Ma, R., 2014a. An EOF-based algorithm to estimate chlorophyll a concentrations in Taihu Lake from MODIS land-band measurements: Implications for near real-time applications and forecasting models. Remote Sens. 6, 10694–10715.

Qi, L., Hu, C., Duan, H., Cannizzaro, J., Ma, R., 2014b. A novel MERIS algorithm to derive cyanobacterial phycocyanin pigment concentrations in a eutrophic lake: Theoretical basis and practical considerations. Remote Sens. Environ. 154, 298–317.

Qi, L., Hu, C., Duan, H., Zhang, Y., Ma, R., 2015. Influence of particle composition on remote sensing reflectance and MERIS maximum chlorophyll index algorithm: Examples from Taihu Lake and Chaohu Lake. IEEE Geosci. Remote Sens. Lett. 12, 1170–1174.

Qin, B., Xu, P., Wu, Q., Luo, L., Zhang, Y., 2007. Environmental issues of Lake Taihu, China. Hydrobiologia 581, 3–14.

Qin, B., Zhu, G., Gao, G., Zhang, Y., Li, W., Paerl, H.W., Carmichael, W.W., 2010. A drinking water crisis in Lake Taihu, China: Linkage to climatic variability and lake management. Environ. Manag. 45, 105–112.

Qin, P., Simis, S.G., Tilstone, G.H., 2017. Radiometric validation of atmospheric

correction for MERIS in the Baltic Sea based on continuous observations from ships and AERONET-OC. Remote Sens. Environ. 200, 263–280.
Shi, Y., Shen, Y., Kang, E., Li, D., Ding, Y., Zhang, G., Hu, R., 2007. Recent and future climate change in Northwest China. Clim. Chang. 80, 379–393.
Shi, K., Zhang, Y., Zhu, G., Liu, X., Zhou, Y., Xu, H., Qin, B., Liu, G., Li, Y., 2015. Long-term remote monitoring of total suspended matter concentration in Lake Taihu using 250m MODIS-aqua data. Remote Sens. Environ. 164, 43–56.
Shu, J., 1993. Assessment of eutrophication in main lakes of China. Oceanol. Limnol. Sin. 24, 616–620.
Smith, M.E., Lain, L.R., Bernard, S., 2018. An optimized chlorophyll a switching algorithm for MERIS and OLCI in phytoplankton-dominated waters. Remote Sens. Environ. 215, 217–227.
Song, K., Lin, L., Tedesco, L.P., Shuai, L., Duan, H., Liu, D., Hall, B.E., Jia, D., Li, Z., Shi, K., 2013. Remote estimation of chlorophyll-a in turbid inland waters: Three-band model versus GA-PLS model. Remote Sens. Environ. 136, 342–357.
Soomets, T., Uudeberg, K., Jakovels, D., Brauns, A., Zagars, M., Kutser, T., 2020. Validation and comparison of water quality products in Baltic lakes using sentinel-2 MSI and sentinel-3 OLCI data. Sensors 20, 742.
Steinmetz, F., Ramon, D., 2018. Sentinel-2 MSI and Sentinel-3 OLCI consistent ocean colour products using POLYMER. In: Remote Sensing of the Open and Coastal Ocean and Inland Waters. International Society for Optics and Photonics, pp. 107780E.
Steinmetz, F., Deschamps, P.-Y., Ramon, D., 2011. Atmospheric correction in presence of sun glint: Application to MERIS. Opt. Express 19, 9783–9800.
Steinmetz, F., Ramon, D., Deschamps, P., 2016. ATBD V1—Polymer atmospheric correction algorithm. In: Technical Report.
Su, J., Xuan, W., Zhao, S., Chen, B., Yang, Z., 2015. A structurally simplified hybrid model of genetic algorithm and support vector machine for prediction of chlorophyll a in reservoirs. Water 7, 1610–1627.
Sun, D.Y., Li, Y.M., Wang, Q., 2009. A unified model for remotely estimating chlorophyll a in Lake Taihu, China, based on SVM and in situ hyperspectral data. IEEE Trans. Geosci. Remote Sens. 47, 2957–2965.
Tang, Q., Bao, Y., He, X., Fu, B., Collins, A.L., Zhang, X., 2016. Flow regulation manipulates contemporary seasonal sedimentary dynamics in the reservoir fluctuation zone of the Three Gorges Reservoir, China. Sci. Total Environ. 548–549, 410–420.
Tao, S., Fang, J., Zhao, X., Zhao, S., Shen, H., Hu, H., Tang, Z., Wang, Z., Guo, Q., 2015. Rapid loss of lakes on the Mongolian Plateau. Proc. Natl. Acad. Sci. U. S. A. 112, 2281–2286.
Vicent, J., Sabater, N., Tenjo, C., Acarreta, J.R., Manzano, M., Rivera, J.P., Jurado, P., Franco, R., Alonso, L., Verrelst, J., 2016. FLEX end-to-end mission performance simulator. IEEE Trans. Geosci. Remote Sens. 54, 4215–4223.
Wang, G.T., 2019. China's Population: Problems, Thoughts and Policies. Routledge.
Wang, S., Yan, F., Yi, Z., Zhu, L., Wang, L., Jiao, Y., 2005. Water quality monitoring using hyperspectral remote sensing data in Taihu Lake China. In: IEEE International Geoscience & Remote Sensing Symposium.
Wang, M., Shi, W., Tang, J., 2011. Water property monitoring and assessment for China's inland Lake Taihu from MODIS-aqua measurements. Remote Sens. Environ. 115, 841–854.
Wang, J., Sheng, Y., Tong, T.S.D., 2014. Monitoring decadal lake dynamics across the Yangtze Basin downstream of Three Gorges Dam. Remote Sens. Environ. 152, 251–269.
Wang, W., Liu, X., Wang, Y., Guo, X., Lu, S., 2016. Analysis of point source pollution and water environmental quality variation trends in the Nansi Lake basin from 2002 to 2012. Environ. Sci. Pollut. Res. Int. 23, 4886–4897.
Warren, M.A., Simis, S.G.H., Martinez-Vicente, V., Poser, K., Bresciani, M., Alikas, K., Spyrakos, E., Giardino, C., Ansper, A., 2019. Assessment of atmospheric correction algorithms for the sentinel-2A MultiSpectral Imager over coastal and inland waters. Remote Sens. Environ. 225, 267–289.
Wei, J., Lee, Z., Shang, S., 2016. A system to measure the data quality of spectral remote-sensing reflectance of aquatic environments. J. Geophys. Res. Oceans 121, 8189–8207.
Wu, G., De Leeuw, J., Skidmore, A.K., Prins, H.H.T., Liu, Y., 2008. Comparison of MODIS and Landsat TM5 images for mapping tempo–spatial dynamics of Secchi disk depths in Poyang Lake National Nature Reserve, China. Int. J. Remote Sens. 29, 2183–2198.
Xiao, Y., Ferreira, J.G., Bricker, S.B., Nunes, J.P., Zhu, M., Zhang, X., 2007. Trophic assessment in Chinese coastal systems-review of methods and application to the Changjiang (Yangtze) Estuary and Jiaozhou Bay. Estuar. Coasts 30, 901–918.
Xiao, X., Zhang, T., Zhong, X., Shao, W., Li, X., 2018. Support vector regression snow-depth retrieval algorithm using passive microwave remote sensing data. Remote Sens. Environ. 210, 48–64.
Xie, J., Wang, X., Zhang, J., Li, W., 2010. Analysing Developing Trend of Chlorophyll-a Concentration in Chaohu Lake Based on TM/ETM∼+ Image. China Environ. Sci. 30, 677–682.
Xu, X., Wang, Y., 2017. Study on spatial spillover effects of logistics industry development for economic growth in the Yangtze River Delta City cluster based on spatial Durbin Model. Int. J. Environ. Res. Public Health 14.
Xu, H., Paerl, H.W., Qin, B., Zhu, G., Gaoa, G., 2010. Nitrogen and phosphorus inputs control phytoplankton growth in eutrophic Lake Taihu, China. Limnol. Oceanogr. 55, 420–432.
Xue, K., Ma, R., Wang, D., Shen, M., 2019. Optical classification of the remote sensing reflectance and its application in deriving the specific phytoplankton absorption in optically complex lakes. Remote Sens. 11, 184.
Yang, X., Anderson, N.J., Dong, X., Shen, J.I., 2008. Surface sediment diatom assemblages and epilimnetic total phosphorus in large, shallow lakes of the Yangtze floodplain: Their relationships and implications for assessing long-term eutrophication. Freshw. Biol. 53, 1273–1290.
Yang, W., Ma, R., Matsushita, B., Chen, J., Fukushima, T., 2010a. An enhanced three-band index for estimating chlorophyll-a in turbid case-II waters: Case studies of Lake Kasumigaura, Japan, and Lake Dianchi, China. IEEE Geosci. Remote Sens. Lett. 7, 655–659.
Yang, Y., Yan, B., Shen, W., 2010b. Assessment of point and nonpoint sources pollution in Songhua River Basin, Northeast China by using revised water quality model. Chin. Geogr. Sci. 20, 30–36.
Yin, H., Liu, G., Pi, J., Chen, G., Li, C., 2007. On the river–lake relationship of the middle Yangtze reaches. Geomorphology 85, 197–207.
Yuan, G.L., Liu, C., Chen, L., Yang, Z., 2011. Inputting history of heavy metals into the inland lake recorded in sediment profiles: Poyang Lake in China. J. Hazard. Mater. 185, 336–345.
Zhang, Z.S., Mei, Z.P., 1996. Effects of human activities on the ecological changes of lakes in China. GeoJournal 40, 17–24.
Zhang, J., Liu, S.M., Ren, J.L., Wu, Y., Zhang, G.L., 2007. Nutrient gradients from the eutrophic Changjiang (Yangtze River) Estuary to the oligotrophic Kuroshio waters and re-evaluation of budgets for the East China Sea shelf. Prog. Oceanogr. 74, 449–478.
Zhang, B., Li, J., Shen, Q., Chen, D., 2008a. A bio-optical model based method of estimating total suspended matter of Lake Taihu from near-infrared remote sensing reflectance. Environ. Monit. Assess. 145, 339–347.
Zhang, R., Wu, F., Liu, C., Fu, P., Li, W., Wang, L., Liao, H., Guo, J., 2008b. Characteristics of organic phosphorus fractions in different trophic sediments of lakes from the middle and lower reaches of Yangtze River region and Southwestern Plateau, China. Environ. Pollut. 152, 366–372.
Zhang, Y., Ma, R., Zhang, M., Duan, H., Loiselle, S., Xu, J., 2015. Fourteen-year record (2000 − 2013) of the spatial and temporal dynamics of floating algae blooms in Lake Chaohu, observed from time series of MODIS images. Remote Sens. 7, 10523–10542.
Zhang, M., Zhang, Y., Yang, Z., Wei, L., Yang, W., Chen, C., Kong, F., 2016. Spatial and seasonal shifts in bloom-forming cyanobacteria in Lake Chaohu: Patterns and driving factors. Phycol. Res. 64, 44–55.
Zhang, M., Hu, C., Cannizzaro, J., English, D., Barnes, B.B., Carlson, P., Yarbro, L., 2018. Comparison of two atmospheric correction approaches applied to MODIS measurements over North American waters. Remote Sens. Environ. 216, 442–455.
Zhao, S., Fang, J., Miao, S., Gu, B., Tao, S., Peng, C., Tang, Z., 2005. The 7-decade degradation of a large freshwater lake in Central Yangtze River, China. Environ. Sci. Technol. 39, 431–436.
Zhu, Q., Li, J., Zhang, F., & Qian, S. (2017). Distinguishing cyanobacterial bloom from floating leaf vegetation in Lake Taihu based on Medium-Resolution Imaging Spectrometer (MERIS) data. IEEE J. Select. Topics Appl. Earth Observ. Remote Sens., PP, 1–11.
Zurita-Milla, R., Clevers, J.G.P.W., Schaepman, M.E., Kneubuehler, M., 2010. Effects of MERIS L1b radiometric calibration on regional land cover mapping and land products. Int. J. Remote Sens. 28, 653–673.